Additive-manufacturing repair towards restoring fatigue performance of metallic component: experiment and phase-field model prediction

Additive-manufacturing repair towards restoring fatigue performance of metallic component: Experiment and phase-field model prediction

Wei Tang[a,d], Lingfeng Wang[b], Shen Sun[a], Liucheng Zhou[c], Marco Paggi[d], Min Yi[a,*]

[a]*State Key Laboratory of Mechanics and Control for Aerospace Structures & Institute for Frontier Science & College of Aerospace Engineering, Nanjing University of Aeronautics and Astronautics (NUAA), Nanjing 210016, China*
[b]*Jiangsu Aero-XY Technology Co., Ltd, Wuxi 214000, China*
[c]*National Key Lab of Aerospace Power System and Plasma Technology, Air Force Engineering University, Xi'an 710038, China*
[d]*IMT School for Advanced Studies Lucca, Piazza San Francesco 19, Lucca, 55100, Italy*

Abstract

Laser additive manufacturing (LAM) is increasingly employed as an in-situ repair technique for restoring the structural integrity and fatigue performance of metallic components. The fatigue and fracture behavior of LAM repaired components are significantly affected by defects introduced during the repair process, which poses challenges for predicting fatigue properties after LAM repair. Herein, we demonstrate the fatigue strength enhancement and fatigue crack growth (FCG) mechanisms in LAM repaired titanium-alloy blades by integrating vibration-based bending fatigue experiments with phase-field modeling (PFM). It is found that LAM repair of the notched TC17 forged blade could improve the fatigue strength by 94%. Fatigue cracks are revealed to initiate at internal defects within the LAM repair and propagate along transgranular paths influenced by defect clusters, deviating from the surface-initiated cracks in the forged counterparts. X-ray computed tomography reveals that the defect is dominated by small pores, with over 90% exhibiting an equivalent diameter below 60 μm. Furthermore, a macroscopic PFM incorporating fatigue life model that considers repair-induced pore defects is applied to predict the fatigue performance after LAM repair. Phase-field simulation results are shown to agree well with the experimental ones in terms of fatigue strength (error < 11%), critical crack length (error < 8%), and fracture surface morphology. Our work highlights the governing role of LAM repair-induced pore defects in high-cycle fatigue performance and enables a predictive PFM framework applicable to the fatigue evaluation of LAM repaired metallic components.

Keywords: Additive manufacturing repair; Fatigue strength; Fatigue crack growth; Phase-field model; Compressor blade

1. Introduction

Laser additive manufacturing (LAM) repair has emerged as a widely adopted technique for restoring the structural integrity and service performance of components damaged by foreign object damage (FOD), leveraging the precision and flexibility offered by advanced manufacturing technologies (Denkena et al., 2015; Sarkar et al., 2022; Tomlinson et al., 2023). The LAM repair process utilizes high-energy lasers to melt and fuse metal powders layer by layer, thereby restoring geometric accuracy, reducing local stress concentration, and consequently prolonging fatigue life. Recently, LAM repair has been applied to a variety of engineering alloys and structural parts, including aero-engine blades (Mudge and Wald, 2007; Sun et al., 2015), railway wheels (Zhu et al., 2019), and high-performance steels such as AISI 4340 (Sun et al., 2014), AerMet 100 (Lourenço et al., 2016; Walker et al., 2017), as well as titanium alloys

*Corresponding author
Email address: yimin@nuaa.edu.cn (Min Yi)

TA15 (Zhou et al., 2022, 2024), TC4 (Paydas et al., 2015), and TC17 (Liu et al., 2016; Wang et al., 2024), especially for aerospace components sustaining cyclic loads (Nagalingam et al., 2023; Wang et al., 2023a).

Despite the potential benefits of LAM repair, the fatigue performance of repaired components remains complex, governed by the interplay between microstructural heterogeneity, defect morphology, and fatigue crack growth (FCG) mechanisms (Chen et al., 2024). Zhu et al. (2019) observed the formation of large, deep cracks at the interface between the repair and substrate zones, which were attributed to defects induced by the LAM repair. Wang et al. (2024) investigated the effects of the LAM repair-induced microstructure, residual stress, and defects on high-cycle fatigue performance of TC17 titanium alloy. In the presence of defects, the influence of residual stress is negligible, while pore defects play a dominant role in governing the FCG behavior of the repaired specimens. Such defects act as stress concentrators, facilitating early crack initiation and reducing overall fatigue resistance. Fatigue cracks are often observed to nucleate and propagate rapidly within the LAM repair zone, where reduced ductility and localized plasticity promote damage accumulation. Although the LAM repair offers the potential to improve fatigue life, this benefit is usually compromised by the presence of critical defects (Ling et al., 2024; Molina et al., 2021), highlighting the challenge of reliably predicting the fatigue performance of repaired components.

To clarify the role of defects in fatigue and fracture behavior of LAM repaired components, comprehensive experimental and simulation-based analyses/predictions are required. Most existing numerical studies have focused on statics and thermal analyses during the LAM repair process (Tran et al., 2017; Zhan et al., 2019), while only a limited number of studies have addressed the fatigue and fracture behavior of LAM repaired specimens. Molina et al. (2021) predicted the fatigue life of LAM repaired steel components using a fracture mechanics approach that considers hardness gradient, defect size and residual stress. Both experimental and numerical results indicate that the improvement in the fatigue life provided by the LAM repair can be diminished by large defects, highlighting the importance of eliminating defects during the repair process. Conventional methods for predicting fatigue life and FCG behavior, including energy dissipation method (Mi et al., 2025), fractal approach (Jones et al., 2016; Plekhov et al., 2011), fracture mechanics approach (Molina et al., 2021), cohesive zone models (Jie et al., 2021), crystal plasticity models (Hu and Yi, 2024; Li et al., 2022b; Xu et al., 2024; Zan et al., 2025) and extended finite element method (Talebi and Abedian, 2016; Xie et al., 2025), present several limitations. Within these methods, the initial crack, defect geometry, and crack path have to be known as a priori or described with additional elements or enriched ansatz functions. Phase-field model (PFM) has attracted considerable attention as a variational approach for simulating fatigue and fracture behavior, owing to its inherent ability to capture both crack initiation and propagation without additional conditions (Bourdin et al., 2000; Cui et al., 2022; Miehe et al., 2010; Sun et al., 2024).

More recently, PFM has been extended to fatigue, one of the most prevalent material failure mechanisms in structural engineering. Alessi et al. (2018) and Carrara et al. (2020) proposed a variational fatigue PFM, introducing a dissipation potential dependent on strain history and a fatigue degradation function that phenomenologically reduces fracture toughness at the local level. Kalina et al. (2020, 2023) and Tang et al. (2025, 2023, 2024) developed an efficient fatigue fracture phase-field framework by leveraging the power of classical fatigue theories, in which accumulated fatigue damage history is evaluated using the local stress-strain approach (LSA). However, phase-field simulations for fatigue fracture in LAM repaired components have not yet been reported. The LAM repaired process shares similarities with AM and surface treatment process. Existing phase-field studies have primarily addressed the plastic and fracture (Li et al., 2022a; Mattey et al., 2023), hot cracking in AM process (Darabi et al., 2024, 2025; Ruan et al., 2023), anisotropic fracture behavior in AM 316L (Li et al., 2023a, 2021), and AM 6061 aluminium (Ge et al., 2023). To consider the AM-induced microstructural orientation, Li et al. (2023a, 2022a, 2025) developed a PFM framework integrating transversely isotropic Hill48 and modified Mohr-Coulomb constitutive models to depict the plastic and fracture behaviours of AM metallic materials. Besides, Tang et al. (2025) and Sun et al. (2025) considered residual stress effect and predicted the fatigue life and FCG behavior in laser shock peened specimens and compressor blade through PFM. These studies overlook the role of defects, which critically influence the fatigue and

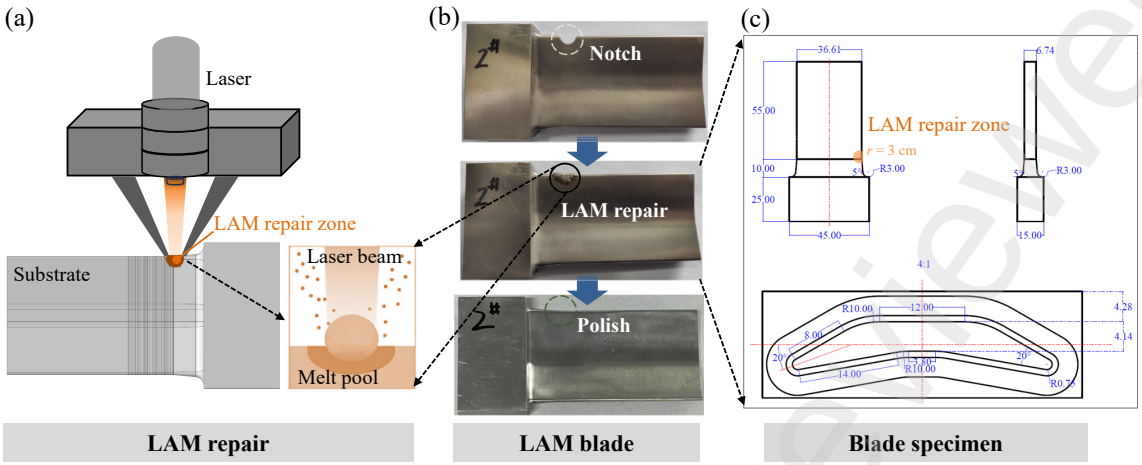

Fig. 1. (a) Laser additive manufacturing (LAM) repair processes and simulated titanium-alloy compressor blades. (b) LAM is used to repair the leading edge of blade notch, followed by polishing to make the repaired area's surface matched the original state. (c) Blade specimen geometry.

fracture behavior of LAM repaired components (Lourenço et al., 2016; Walker et al., 2017; Zhu et al., 2019). Defects have received increasing attention in material fracture and failure. The void evolution and spalling damage of ductile materials under high-velocity impacts (Han et al., 2024) are investigated by Gurson-type PFM. Cavuoto et al. (2024) considered the impact of multiscale porosity on the failure of ceramics, with meso and macro porosity incorporated into the PFM. Loiodice et al. (2025) investigated the AM-induced pore defects' influence on near threshold FCG behavior using crystal plasticity model. Although these models are capable of capturing brittle and ductile fracture behaviors in porous specimens, they fall short in accurately assessing the fatigue life of LAM repaired components subjected to high-cycle loading. Lately, fatigue life models have been proposed to incorporate defect features such as size, location, and sphericity, including models based on ΔK (Murakami et al., 1989; Murakami and Usuki, 1989), Z (Liu et al., 2023; Zhu et al., 2018), X (Hu et al., 2021), T (Li et al., 2023b), and $\Delta\Omega$ (Wang et al., 2023b)–N_f formulations. These empirical models have demonstrated success in reducing the scatter of fatigue data and improving fatigue life prediction accuracy in AM components.

This work aims to decipher the defect-sensitive fatigue and fracture behavior in LAM repaired components through a combination of experiments and phase-field model. Vibration-based bending fatigue tests, scanning electron microscopy (SEM) and X-ray computed tomography (X-CT) scans are conducted to characterize fatigue performance and crack/defect morphology. Furthermore, a macroscopic PFM incorporating fatigue life model that considers LAM repair-induced pore defects is applied to predict fatigue crack initiation, growth, and fatigue life in LAM repaired specimens and components. The good agreement between phase-field predictions and experimental results validates the predictive capability of the proposed PFM framework. The manuscript is organized as follows. Sect. 2 describes the experimental procedures, including bending fatigue tests, SEM and X-CT scans on LAM repaired titanium-alloy blades. In Sect. 3, we present the details on the phase-field fatigue fracture model, with an emphasis on incorporating fatigue life model that considers LAM repair-induced pore defects. We then in Sect. 4 investigate the pore defects distribution, fatigue and fracture behavior, and failure mechanism of LAM repaired titanium-alloy blades. Finally, Sect. 5 gives the conclusive summary.

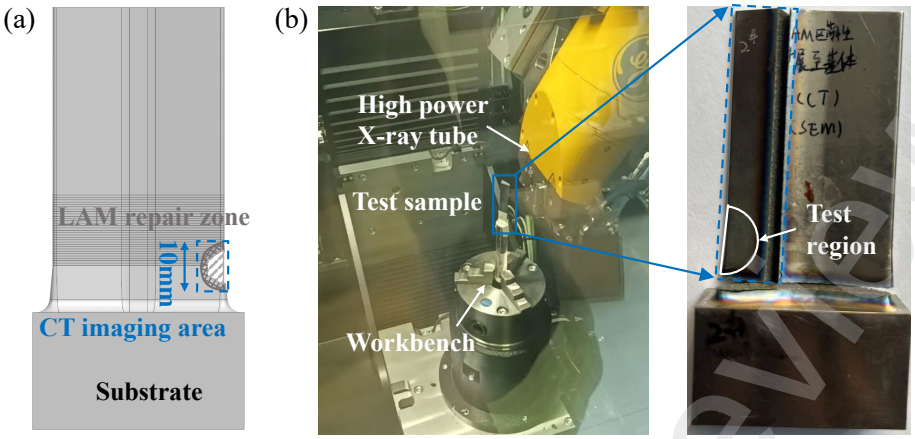

Fig. 2. Defect characterization of the LAM repair blade: (a) X-CT scan imaging; (b) scanning chamber with the corresponding test region.

2. Experimental procedures

2.1. Materials and laser additive manufacturing repair

The substrate of the simulated compressor blade is manufactured by forge TC17 titanium alloy. Details of the heat treatment, mechanical properties and microstructure of TC17 alloy can be found in a previous study (Wang et al., 2024). The blade is first prefabricated with an artificial notch, then repaired using LAM, and finally polish to restore its original geometry and surface roughness, as shown in Fig. 1 The LAM is performed using a coaxial powder feeding method on a BLT-C400 type metal AM system (Platinum, China). TC17 titanium alloy powder produced by the plasma rotating electrode processing method is used in the LAM repair process, with particle sizes ranging from 53 to 180 μm. To accommodate the geometric complexity of actual engine blades, a simulated leading-edge blade was designed based on the geometry and stress distribution near the leading edge of a first-stage fan rotor. The LAM repair system consists a high-power laser, a dual-channel constant flow powder feeder, a four-channel powder nozzle, and a three-axis computer numerical control workbench. High-purity argon gas is used to deliver the powder and to maintain an inert atmosphere within the processing chamber. The process utilized coaxial powder feeding, with high-purity argon gas used to transport the powder, and the processing is conducted in an argon atmosphere chamber. The LAM repair parameters are: the powder feed rate is 3 g/min, the laser power is set to 350 W, the spot diameter is 1.6 mm, the scanning speed is 6 mm/s, the overlapping rate is 50%, and the argon flow rate is maintained at 30 L/min.

Considering the actual damage conditions of aircraft engine fan blades, a semicircular notch with a 3 mm radius, located 10 mm from the clamping end, is introduced into the blades to simulate FOD. After LAM repair, the surface of each blade is post-processed through grinding, manual sanding, and final polishing to restore its original. The target surface roughness is grade 9 (Ra = 0.4 μm), which is critical for minimizing stress concentrations and mitigating fatigue failure initiated by surface irregularities.

2.2. Pore defects characterization

Global defect characterization is carried out on LAM repair TC17 titanium alloy leading-edge simulated blades using a Phoenix v-tome-x M computed tomography system. The defect scanning schematic is shown in Fig. 2. To balance imaging fidelity and cost, one representative specimen was scanned using high-resolution CT with a voxel size of 6.47 μm, a focal spot size of 13.125 μm, a photon energy of 60 keV, a voltage of 125 kV, a current of 105 μA, and an exposure time of 500 ms. A 0.4 mm copper filter was applied, with an imaging range of 20 mm and a scan interval of 5.8 μm. The remaining simulated blades were characterized at lower resolution (10 μm).

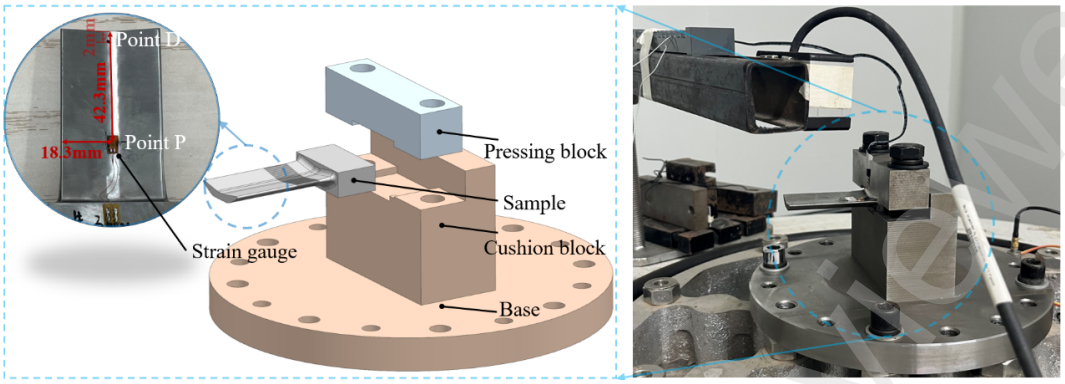

Fig. 3. Vibration-based bending fatigue test of LAM repaired TC17 simulated compressor blade.

2.3. Vibration-based bending fatigue

Vibration-based bending fatigue tests with a stress ratio of $R = -1$ are conducted using a digital electrodynamic vibration testing system (ES-50-445, Dongling, China), as shown in Fig. 3. The step-loading method is employed to evaluate the high-cycle fatigue strength of unrepair and LAM repair TC17 simulated blades, with a maximum cycle of 3×10^7. The fatigue tests are conducted on 12 unrepaired TC17 blades and 12 LAM repaired blades with an initial 3 mm-depth semicircular notch. For the LAM repaired blades, which exhibit large fatigue scatter, the initial maximum stress is set to 150 MPa. The load increment is 15 MPa for the first six stages and increases to 25 MPa from the seventh stage onward (i.e., starting at 240 MPa).

Based on the step-loading method (Maxwell and Nicholas, 1999), the fatigue strength corresponding to the given number of cycles can be calculated as, i.e.,

$$\sigma_e = \sigma_p + (\sigma_f - \sigma_p)\frac{n}{N}, \tag{1}$$

where σ_e is the fatigue strength corresponding to the given number of cycles, σ_p is the maximum stress level of the previous stress step, σ_f is the maximum stress level of the final (failure) step, n is the number of cycles to failure in the final step, and N is the predetermined number of cycles per step.

3. Phase-field fatigue fracture model considering LAM repair-induced pore defects

In this section, we present the phase-field fatigue fracture model for LAM repair component, the finite element (FE) model setup, and the verification of predictive results against experiments. The simulation framework incorporates a pore-defect informed PFM for fatigue fracture, along with relevant implementation details. The PFM considers a fatigue-life model that accounts for defect size, location, and sphericity in LAM repair components, and establishes a correlation between LAM repair-induced defect features and fatigue life, with calibration based on experimental S–N data from LAM repair specimens and components.

Overall, the experimental and simulation workflow is summarized in Fig. 4. First, the parameters of the fatigue life model considering LAM repair-induced pore defects are calibrated based on fatigue data of LAM repaired standard tensile fatigue specimen. Subsequently, vibration-based bending fatigue tests, X-CT, and SEM scans are performed on the LAM repair blades to investigate its defects distribution, fatigue strength and FCG behavior. Meanwhile, the experimentally characterized defect parameters are used as inputs for phase-field fatigue fracture model to predict the fatigue strength and FCG behavior of LAM repair blades. The predictive capability of the phase-field simulation is validated through comparison with experimental observations.

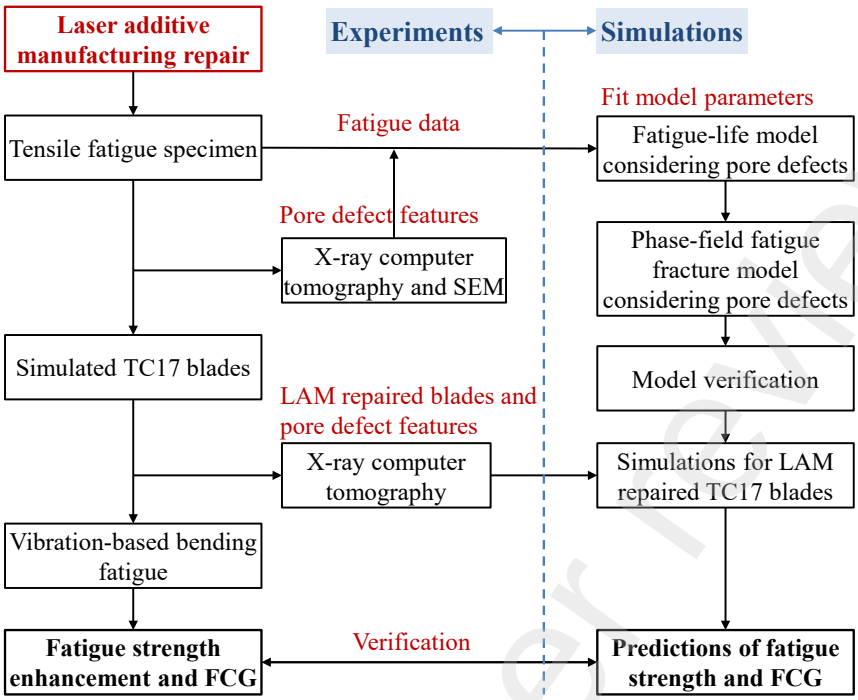

Fig. 4. Flowchart for the experimental and phase-field simulation procedures investigating the fatigue and fracture behavior of LAM repaired blade.

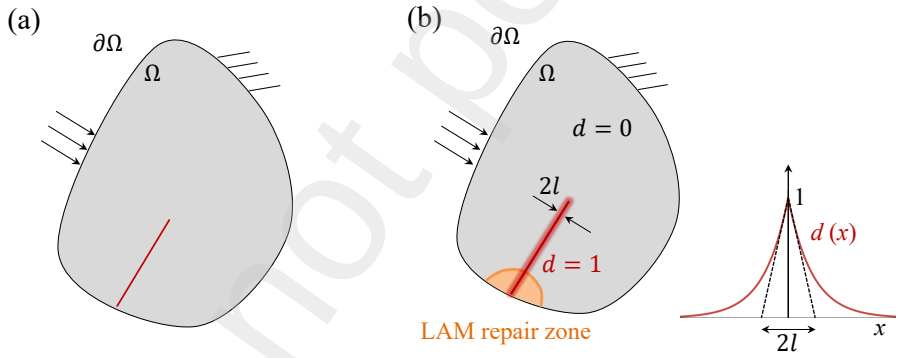

Fig. 5. Regularized representation of (a) Discrete crack and (b) Diffusive crack.

3.1. Phase-field model

An arbitrary fractured body Ω with an evolving crack surface Γ containing a crack defined by the internal boundary is considered. Based on the variational framework outlined in (Bourdin et al., 2000), the total energy functional Π can be expressed as:

$$\Pi = \int_{\Omega} \psi_e(\varepsilon, d)\mathrm{d}V + \int_{\Omega} \psi_f(d)\mathrm{d}V - \int_{\Omega} \boldsymbol{b}\cdot\boldsymbol{u}\mathrm{d}V - \int_{\partial\Omega} \boldsymbol{t}\cdot\boldsymbol{u}\mathrm{d}A, \tag{2}$$

where $\boldsymbol{u}$ and d are the displacement and crack field variables, respectively. Here, $\psi_e(\varepsilon, d)$ denotes the elastic strain energy density of the damaged solid and $\psi_f(d)$ represents the dissipative fracture energy, $\boldsymbol{b}$ is the external body force, $\boldsymbol{t}$ corresponds to the external surface traction. From the assumption of small strains, the strain tensor is defined as $\varepsilon = 1/2(\nabla\boldsymbol{u} + \nabla\boldsymbol{u}^T)$. The order parameter $d \in [0, 1]$ represents the diffusive crack, transitioning smoothly from $d = 0$

for the intact state to $d = 1$ for the broken material state, as shown in Fig. 5. For one-dimensional case, this variable can be mathematically expressed using an exponential function as $d(x) = e^{-(|x|/l)}$ (Miehe et al., 2010).

In order to incorporate accumulated fatigue damage into the fracture PFM, a scalar fatigue degradation function $\alpha(D)$ is introduced to lower the fracture toughness G_c locally during cyclic loading (Kalina et al., 2020). It is monotonically decreasing within a damage domain. Also, the elastic strain energy density is regularized by introducing a degradation function $g(d)$ to account for the subsequent loss of stiffness due to damage. In the absence of external forces, the total energy function can be rewritten as (Borden et al., 2016)

$$\Pi = \int_{\Omega} \left[g(d)\psi_{\mathrm{e}}(\varepsilon) + \alpha(D) G_c \gamma(d, \nabla d) \right] \mathrm{d}V. \tag{3}$$

D is a phase-field damage variable that is accumulated strictly locally as a history variable. When $D = 0$, a material point has not undergone any fatigue loads, whereas $D = 1$ indicates that it has reached the maximum load cycles it can bear before losing its integrity, reflecting a fatigue damage cumulation across the entire lifetime (Tang et al., 2024). The degradation function is defined by satisfying the following properties, $g'(d) < 0,\ g(0) = 1,\ g(1) = 0,\ g'(1) = 0$. A general form of $g(d)$ is specified here as $g(d) = (1 - d)^2$.

The volumetric-deviatoric decomposition method (Amor et al., 2009) is adopted to split the elastic energy in the model to avoid compression fatigue failure, i.e.,

$$\psi_e^+(\varepsilon) = \frac{1}{2} K \langle \mathrm{tr}(\varepsilon) \rangle_+^2 + \mu \varepsilon^{\mathrm{D}} \cdot \varepsilon^{\mathrm{D}}, \quad \psi_{el}^-(\varepsilon) = \frac{1}{2} K \langle \mathrm{tr}(\varepsilon) \rangle_-^2, \tag{4}$$

where μ is the shear modulus, K is the bulk modulus, tr and D represent the trace and the deviatoric parts of a tensor, respectively. $\langle \cdot \rangle$ is the Macaulay bracket selecting the positive (negative) part of the argument. The crack surface energy density $\gamma(d, \nabla d)$ is described as

$$\gamma(d, \nabla d) = \frac{1}{2l} d^2 + \frac{l}{2} |\nabla d|^2. \tag{5}$$

where l is a length scale parameter that governs the width of the diffused fracture zone. As $l \to 0$, the PFM transitions from a continuous diffusive field representation to a close approximation of the sharp fracture topology based on Γ-convergence theory (Braides, 1998).

Herein, the fatigue degradation function $\alpha(D)$ reads (Kalina et al., 2020; Tang et al., 2024)

$$\alpha(D) = (1 - \alpha_0)(1 - D)^{\xi} + \alpha_0, \tag{6}$$

where the fatigue degradation parameters ξ controls the relation between D and d. The threshold α_0 represents the residual fracture toughness, which is set larger than zero to ensure a certain resistance against crack propagation at the end of lifetime and numerical convergence. The governing equation for the crack field d is described by Allen–Cahn equation (Miehe et al., 2015), i.e.,

$$\eta \dot{d} - 2(1 - d)\mathcal{H} + \alpha(D) \frac{G_c}{l} (d - l^2 \nabla^2 d) = 0. \tag{7}$$

where η is a non-negative viscosity parameter. We assume a quasi-static fracture in this paper. Crack evolution is an irreversible process. As a consequence, the phase-field evolution law must fulfill the irreversibility condition $\dot{d} \geq 0$. To achieve this, the history variable field $\mathcal{H}$ with respect to the positive strain energy is introduced (Miehe et al., 2010), i.e.,

$$\mathcal{H} = \max_{d \in [0;t]} \psi_{\mathrm{e}}^+(\varepsilon). \tag{8}$$

Then, the phase-field damage variable D is evaluated through the LSA involving the concepts of stress-strain revaluation, S-N curve and linear damage accumulation. Using the Ramberg–Osgood model (Anatolyevich and Yakovlevna, 2019) to revaluate stress and strain for the material's elasto-plastic behavior, i.e.,

$$\varepsilon_{\mathrm{a}} = \frac{\sigma}{E} + \left(\frac{\sigma}{K'} \right)^{1/n'}, \tag{9}$$

with the cyclic strength coefficient K' and cyclic strain hardening exponent n'. Assuming small scale yielding occurs at a notch and the entire component behaves mostly elastic, the cyclic material behavior can be approximated according to Neuber (1961). In accordance with Neuber's rule, the strain energy density for the elastic solution, depending on σ_{el}, $\varepsilon_{\mathrm{el}}$, is assumed to be equal to that of the pseudo-plastic response with σ, ε. Then, ε_a is introduced in ε using Eq. (9), and the revaluation stress-strain pair σ and ε can be solved, i.e.,

$$\sigma_{\mathrm{el}}\varepsilon_{\mathrm{el}} = \sigma\varepsilon. \tag{10}$$

For the fatigue revaluation of LAM repaired specimen, a macroscopic fatigue life model considering pore defects is applied to calculate the lifetime N_i, i.e.,

$$\sigma_{\max} Y \cdot \left[\sqrt{area}\right]^{\mu} \cdot D_L^{\beta}/C_d^{\alpha} = \alpha'(2N_f)^{\beta'} \Leftrightarrow W = \alpha'(2N_f)^{\beta'}, \tag{11}$$

where the defect morphology is simplified as three-dimensional (3D) spherical and cluster defects ($Y = 1$ in this work for 3D facet-type defects). W is a pore defect related fatigue damage parameter. $\sqrt{area}$, D_L, and C_d are the effective area, location, and sphericity of LAM repair-induced defects, respectively, as shown in Fig. 6b. μ, α and β are the material-dependent constants involving defect features. α' and β' are the fitting parameters according to the experimental fatigue data of LAM repaired specimen.

Then, inspired by the linear cumulative damage rule (Miner, 1945), the phase-field damage variable D in Eq. (6) is calculated as

$$D = \sum_i \Delta N \frac{1}{N_i}. \tag{12}$$

where N_i represents the fatigue life during a single loading cycle i. N_f is solved using the fatigue life W–N_f model with Eq. (11). ΔN is a cyclic equivalent factor involving envelope load to accelerate fatigue damage calculation.

3.2. Finite element implementation

Herein, the PFM is solved using the FE method by converting the strong forms of governing equations into weak forms through the introduction of a test function. The displacement u_i ($i = 1, 2, 3$) and the crack phase-field order parameter d are taken as the degrees of freedom. The governing equations of crack evolution and stress balance are reformulated in the weak form over the integral domain, i.e.,

$$\begin{aligned} 0 &= \int_\Omega \sigma_{ij}\phi_{i,j}\mathrm{d}V - \int_{\partial\Omega} \sigma_{ij}n_j\phi_i\mathrm{d}A, \\ 0 &= \int_\Omega \left(\eta\dot{d} - 2(1-d)\mathcal{H} + \alpha(D)\frac{G_c}{l}d\right)\theta\mathrm{d}V + \int_\Omega 2\alpha(D)G_c l\theta_{,i}d_{,i}\mathrm{d}V - \int_{\partial\Omega} 2\alpha(D)G_c l\theta d_{,i}n_i\mathrm{d}A, \end{aligned} \tag{13}$$

where ϕ_i and θ are the test function for u_i and d, respectively. The surface terms $\sigma_{ij}n_j$ in Eq. (13) represent the surface traction conditions. n_i is the normal vector of the boundary $\partial\Omega$. By introducing the shape functions for independent variables and test functions, the discretized form of the equations can be expressed as

$$u_i = N^I u_i^I, \qquad d = N^I d^I, \qquad \dot{d} = N^I \dot{d}_I^I, \qquad \phi_i = N^I \phi_i^I, \qquad \theta = N^I \theta^I, \tag{14}$$

where I denotes the node number. N^I is the shape function. By inserting the discretization into the weak forms, the elemental residuals can be obtained, i.e.,

$$\begin{aligned} R_{u_i}^I &= \int_\Omega \sigma_{ij}N_{,j}^I\mathrm{d}V - \int_{\partial\Omega} N^I\sigma_{ij}n_j\mathrm{d}A, \\ R_d^I &= \int_\Omega \left[N^I\left(\eta\dot{d} - 2(1-d)\mathcal{H} + \alpha(D)\frac{G_c}{l}d\right) + 2\alpha(D)G_c l d_{,i}N_{,i}^I\right]\mathrm{d}V - \int_{\partial\Omega} 2\alpha(D)G_c l N^I d_{,i}n_i\mathrm{d}A. \end{aligned} \tag{15}$$

Regarding time dependence of the residuals, the implicit backward Euler method is employed for time discretization. The residual equation at the current time step t_{n+1} is

$$\underline{\mathbf{R}}^I_{n+1} = \underline{\mathbf{R}}^I\left(\underline{\mathbf{d}}^J_{n+1}, \frac{\underline{\mathbf{d}}^J_{n+1} - \underline{\mathbf{d}}^J_n}{\Delta t}\right), \tag{16}$$

where $(\underline{\mathbf{d}}^J_{n+1} - \underline{\mathbf{d}}^J_n)/\Delta t = \underline{\dot{\mathbf{d}}}^J_{n+1}$ and Δt is time step. $\underline{\mathbf{d}}^J_{n+1}$ should be solved in this equation. For solving these non-linear equations, the Newton iteration scheme is performed at each time step. The corresponding iteration matrix is

$$\underline{\mathbf{S}}^{IJ} = \underline{\mathbf{K}}^{IJ} + \frac{1}{\Delta t}\underline{\mathbf{D}}^{IJ}, \tag{17}$$

where $\underline{\mathbf{K}}^{IJ}$ is the stiffness matrix and $\underline{\mathbf{D}}^{IJ}$ is the damping matrix. After assembling the matrixes, the numerical implementation is conducted within the open source Multiphysics Object Oriented Simulation Environment (Tonks et al., 2012).

3.3. Finite element model setup

The FE model of the LAM repaired TC17 simulated compressor blade is shown in Fig. 6. The 3D FE model of simulated blade is meshed with the 10-node tetrahedral structured element. To reduce computational cost, mesh refinement is applied to the region surrounding the LAM repair zone and the transition section, where cracks are most likely to initiate and propagate. The minimum element size is set to $h_{\min} = 0.2$ mm and phase-field length scale parameter is defined as $l_0 = 0.6$ mm. The FE model is simplified into two material domains: the substrate and the LAM repair zone, as shown in Fig. 6b. Based on the defect characterization, critical defects are located within the LAM repair zone and are identified as the fatigue source. Accordingly, the macroscopic fatigue life model considering pore defect is applied within the LAM repair zone, while the substrate is macroscopically assumed to be defect-free. The loading conditions applied to the compressor blade include both static and cyclic components. Similar to the vibration induced by aerodynamic loads, the cyclic pressure load is applied on the concave of the blade to simulate the reciprocating motion that deviates from the free state. A centrifugal body force corresponding to a rotation speed of 10,000 r/min is applied as a static load. The cyclic load arises from aerodynamic pressure fluctuations, modelled as a sinusoidal pressure with a peak amplitude of 1 MPa and a stress ratio of $R = -1$, as shown in Fig. 6c.

Model and material parameters for the substrate and LAM repair zone of TC17 blade are obtained by tensile fatigue test and defect characterization, as summarized in Table 1. The mechanical properties differ between the substrate and the additively repaired zone of the TC17 blade, with the Young's modulus of the LAM repaired region being lower than that of the substrate. By means of the tensile fatigue data of LAM repaired TC17 specimens, the parameters of the fatigue life model considering LAM repair-induced pore defects are fitted based on the W–N_f curve with Eq. (11), as shown in Fig. 7. It is noted that the substrate region of the LAM repaired TC17 blade is assumed to be defect-free (i.e., defect size equal to zero), while the defect parameters in the LAM repair zone are assigned according to the experimentally measured pore-defect features.

3.4. Phase-field model verification

To verify the PFM, a benchmark comparison of predicted and experimental S–N curves is performed based on the tensile fatigue tests of LAM repaired specimens. The fatigue life of LAM repaired TC17 tensile fatigue specimens under different loads is numerically calculated using the proposed PFM that considers the LAM repair-induced pore defects. The FE model of the LAM repaired TC17 specimen is shown in Fig. 7. Simulations and experiments of LAM repaired TC17 tensile fatigue test are conducted at five maximum stress levels: 250, 300, 350, 400, and 500 MPa, all with a stress ratio of $R = 0.1$. As shown in Fig. 8, the phase-field predicted fatigue life are in good agreement with the experimental results, falling within the ±2 times error band. This indicates that the proposed PFM effectively captures the influence of defects on the fatigue life of LAM repaired standard specimens, yielding highly accurate predictions.

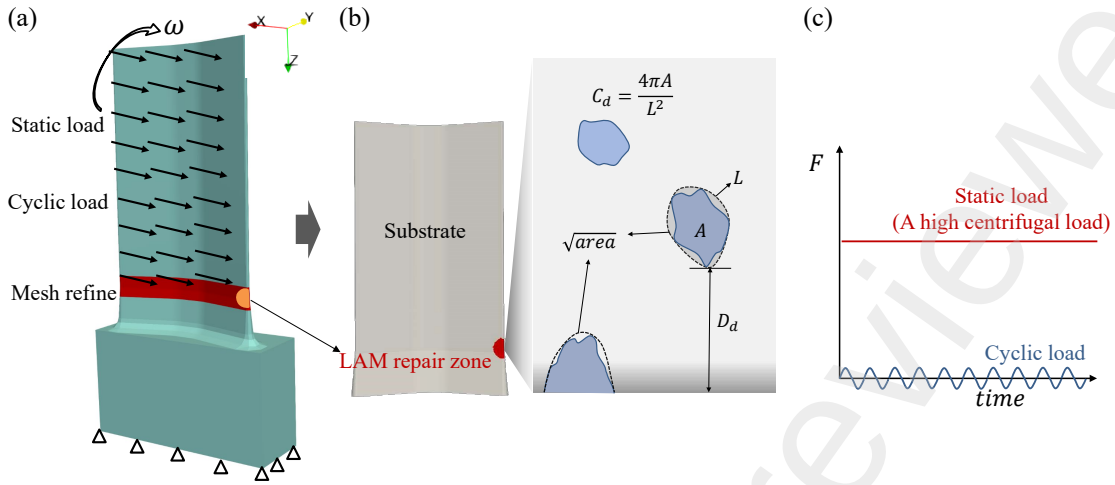

Fig. 6. Simulated compressor blade specimen. (a) Loading setting in the LAM repaired blade; (b) Finite element model of LAM repaired blade including defect features; (c) Loading history including the static load caused by the rotation body force and the cyclic caused by pneumatic pressure.

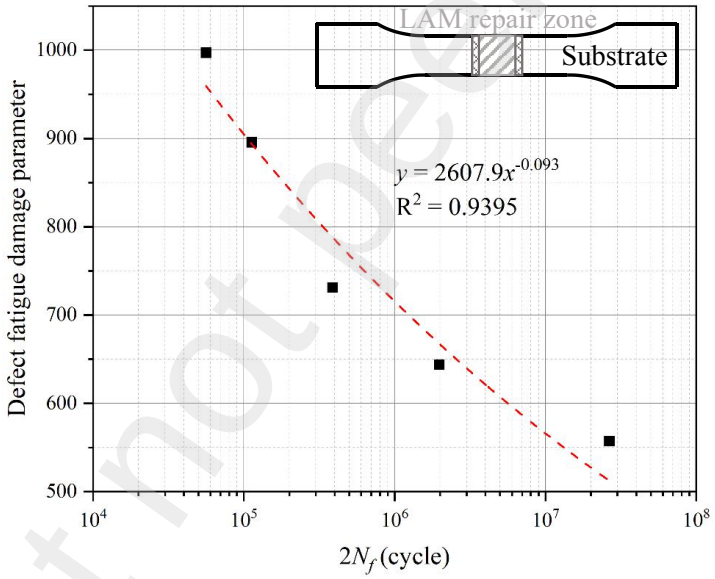

Fig. 7. Experimental fatigue life curve of LAM repaired TC17 tensile fatigue specimen.

4. Experimental and phase-field simulation results

In the following, defect characterization, fatigue fracture characteristics, and fatigue strength of the LAM repaired TC17 blade are discussed by both experimental observations and numerical simulations. The dominant mechanisms underlying fatigue performance restoration through LAM repair are elucidated, and the fatigue life and FCG behavior are predicted using the PFM in Subsection 3.1. For the phase-field simulations of the LAM repaired TC17 blade, the FE model setup and corresponding parameters are provided in Subsection 3.3.

Table 1. Material and simulation parameters of LAM repaired TC17 simulated compressor blade.

Parameter	Name	Unit	Substrate of TC17 blade	LAM repair zone
E	elastic modulus	GPa	112	50
v	poisson ratio	-	0.3	0.3
G_c	fracture toughness	kN/m	21.9	30
η	mobility parameter	-	0.001	0.001
K'	cyclic strength coefficient	GPa	2.754	2.754
n'	cyclic strain hardening exponent	-	0.15	0.15
α	defect sphericity parameter	-	-	0.5
β	defect location parameter	-	-	0.5
μ	defect area parameter	-	-	0.15
α_2	defect-fatigue strength coefficient	GPa· m^x	-	2.608
β_2	defect-fatigue strength exponent	-	-	−0.093

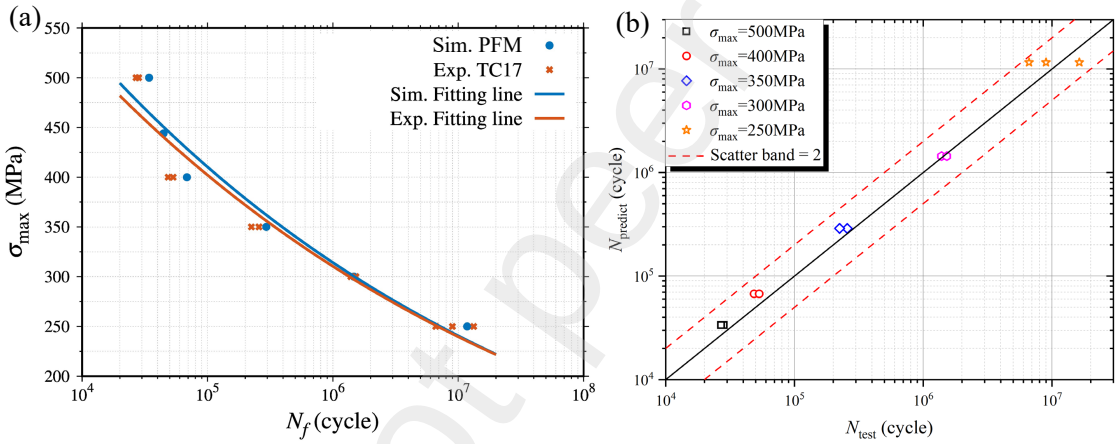

Fig. 8. Fatigue life prediction of LAM repaired TC17 tensile fatigue specimens. (a) Experimental and simulated fatigue life S–N curves; (b) Prediction accuracy analysis.

4.1. Pore defects distribution

Prior to the fatigue tests, X-CT scans are performed to characterize the pore defects distribution in the LAM repaired TC17 blades. The equivalent diameter is defined as the diameter of a sphere having the same volume as the defect, while the sphericity is defined as the ratio between the surface area of such a sphere and that of the actual defect. A sphericity value approaching 1 indicates that the defect approximates a spherical shape. The statistical distributions of equivalent diameter and sphericity are shown in Fig. 9. The equivalent diameter follows a Gaussian distribution with a coefficient of determination (COD) of 0.98, and the sphericity follows a Gaussian distribution with a COD of 0.94. The statistical analysis reveals that the majority of pore defects exhibit ellipsoidal morphologies, characterized by sphericity values exceeding 0.6. Most pore defects possess equivalent diameters smaller than 500 μm, with more than 90% falling below 60 μm. Small, near-spherical pore defects are typically gas pores, whereas larger, more irregular defects are attributed to lack of fusion (LOF) flaws. Fig. 10 summarizes the equivalent diameters and sphericities of the larger pore defects. The maximum observed pore defect diameter is 220 μm, with four pore defects exceeding 100 μm. A generally negative correlation is observed between pore defect size and sphericity: larger pore defects tend to exhibit lower sphericity and more irregular geometries, while smaller pore defects are more

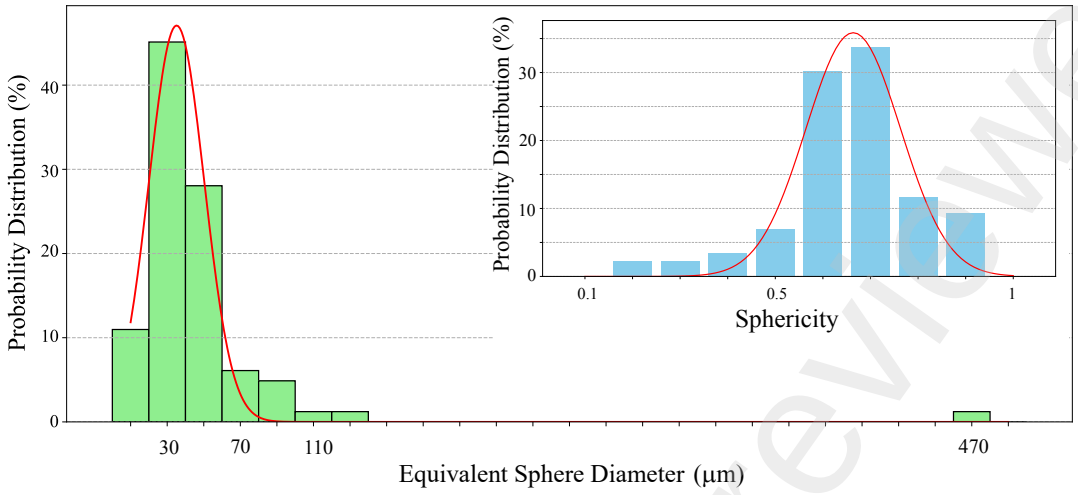

Fig. 9. Statistical distributions of equivalent spherical diameter and sphericity of pore defects in 12 LAM repaired TC17 blades.

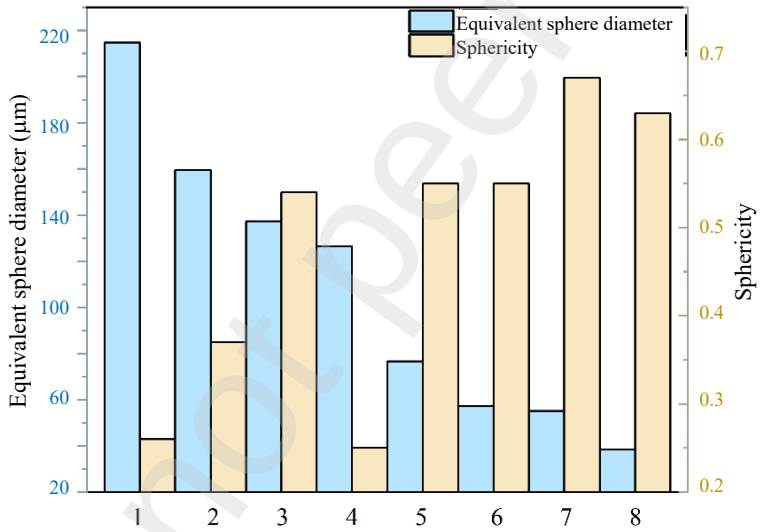

Fig. 10. Pore defect characteristic statistics of equivalent diameter distribution and sphericity distribution in the LAM repaired TC17 blade.

spheroidal in shape (Hu et al., 2020).

Fig. 11 presents the global pore defects characterization results for the LAM repaired TC17 leading-edge simulated blade. From the top view, LAM repair-induced defects are observed in both dot-like and strip-like morphologies, with larger pore defects predominantly located at the bottom of the LAM repair zone, i.e., near the interface between the repair and the substrate. This observation is consistent with the findings from tensile fatigue specimens repaired by LAM (Wang et al., 2024). Fig. 11c shows the front view of the LAM repaired blade, where additional pore defects are detected along the boundary of the LAM repair zone. These pore defects are attributed to uneven heating in the semicircular groove during the LAM repair process, which promotes the formation of pores or LOF flaws near the interface.

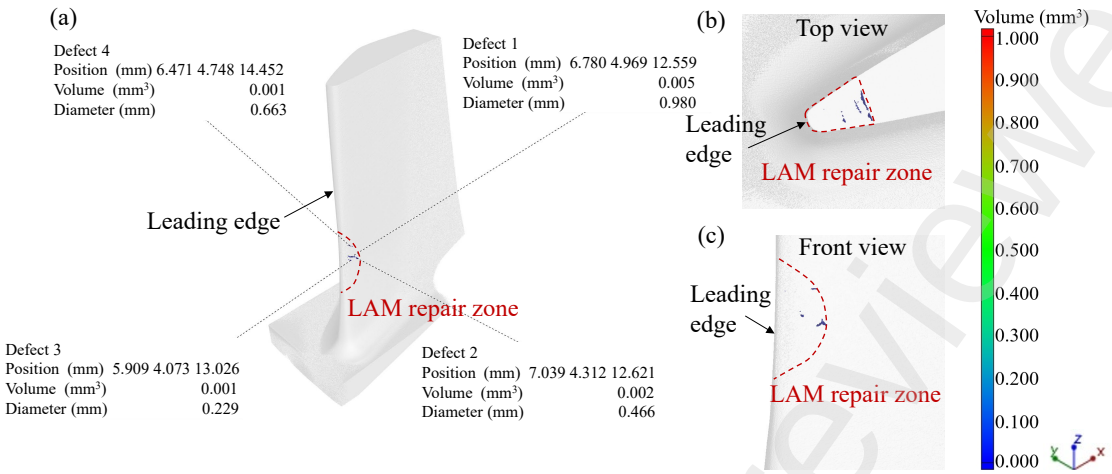

Fig. 11. Defect distributions of the LAM repaired TC17 blade in (a) global view; (b) top view; (c) front view.

4.2. Fatigue fracture characteristics

4.2.1. Fractography

The fracture morphologies of LAM repaired TC17 blade subjected to bending fatigue are observed using SEM, as shown in Fig. 12. A representative blade with a 3 mm semicircular notch repair is initially loaded at 150 MPa and failed after 5.4×10^6 cycles under the maximum stress of 210 MPa. It is observed that cracks initiate at the LAM repair-induced defects near surface, followed by circumferential crack propagation and sudden final fracture. The final fracture surface appeared relatively smooth, with shear lips located near the upper and lower boundaries. The LAM repair zone exhibits surface relief on the fracture surface, while the substrate region exhibited a flat and smooth morphology, highlighting a clear contrast between the two areas. This difference is due to the lower plasticity of the LAM repair zone, which has reduced resistance to plastic deformation under cyclic stress.

As a result, significantly localized plastic flow occurs during crack propagation, forming pronounced ridge patterns and tearing facets. In contrast, the substrate material exhibits better ductility and the final fracture region appears relatively flat. Several fatigue striations oriented perpendicular to the crack path were observed. A magnified view of the initiation zone (Fig. 12b) reveals a few nearby pores, which had minimal influence on the propagation behavior. Tear ridges, elongated facets, and secondary cracks were present on both sides of the LOF, indicating pronounced plastic deformation under cyclic loading. Further magnification reveals cleavage steps near the crack origin.

In the crack propagation region, Fig. 12c shows a rugged surface near the leading edge, marked by tear ridges and parallel cleavage steps (features associated with early-stage growth dominated by localized plasticity). In contrast, the internal fracture surface (Fig. 12d) appears relatively flat, exhibiting abundant river patterns formed by the coalescence of parallel cleavage steps. These step features, formed during crack advancement across cleavage planes of varying height, progressively merged into large clusters, producing characteristic river-like morphologies. At higher magnification, numerous secondary cracks are observed along the crack path, occasionally causing slight deviations in propagation direction.

Fig. 12f shows the fracture illustration of the LAM repaired TC17 compressor blade. Fatigue cracks in the LAM repaired blades tend to initiate at LAM repair-induced defects, e.g., LOF and pores, and then propagate into the substrate. The fatigue striation spacing in the LAM repair zone is noticeably larger than that in the substrate, indicating a faster FCG rate in the LAM repair zone. Additionally, the transient fracture region shows different dimple morphologies between the two zones: the LAM repair zone contains shallow and fine dimples, while the substrate exhibits deeper and coarser ones, suggesting a reduction in ductility due to the additive process. Overall, fatigue cracks in the

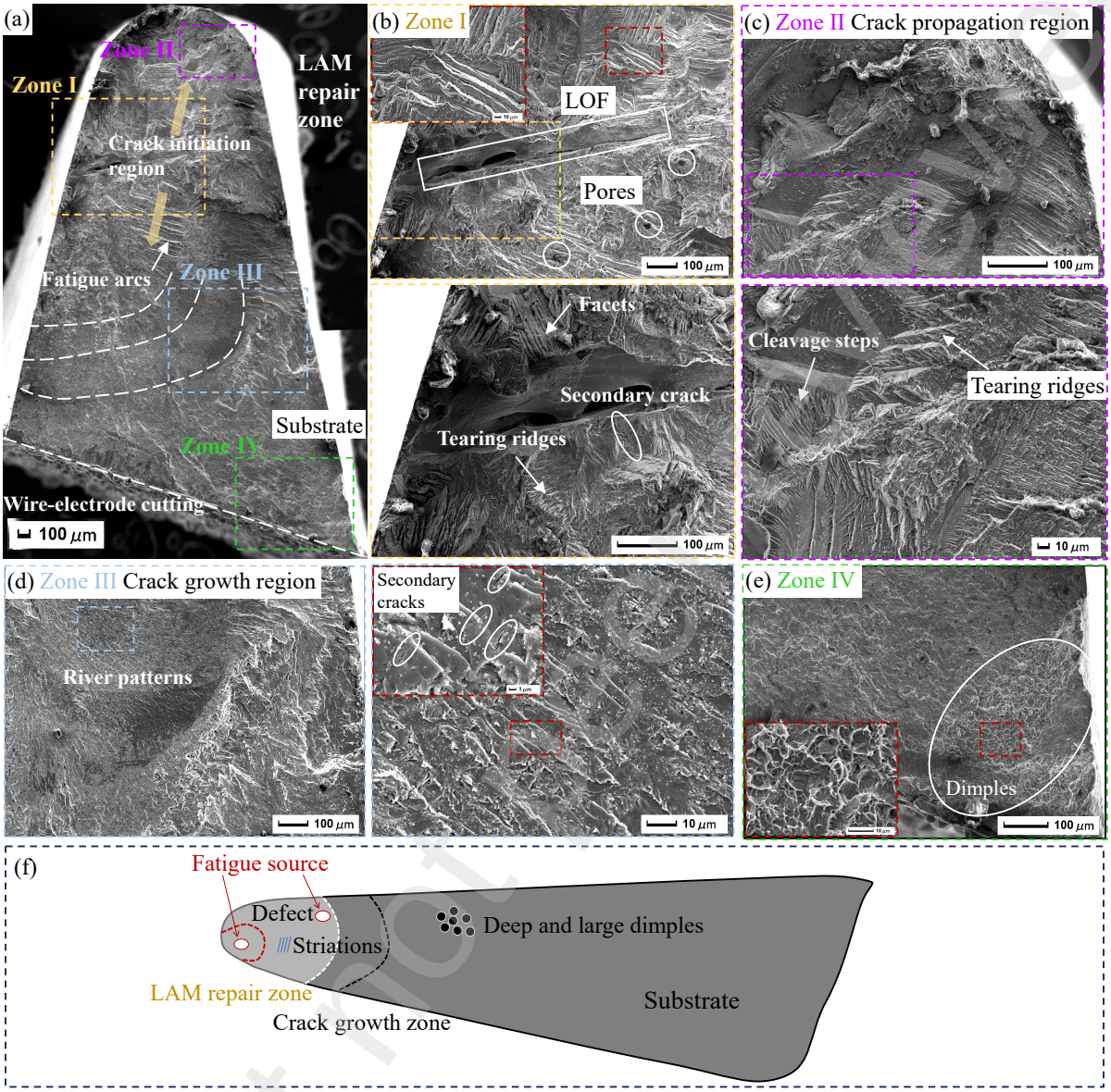

Fig. 12. Fracture morphologies of LAM repaired TC17 simulated compressor blade: (a) Global fracture surface; (b) Crack source and initiation region; (c) Crack growth region; (d) Final fracture region. The specimen is initially loaded at 150 MPa and failed at a loading level of 210 MPa after 5.4×10^6 cycles; (f) Illustration of typical FCG characteristics of LAM repaired TC17 blade.

LAM repaired blade predominantly initiated at pore or LOF defects near the leading edge, contributing to its lower fatigue strength compared to the undamaged forged blade.

4.2.2. Fatigue crack initiation

The distribution of fatigue cracks and internal defects in leading-edge simulated compressor blades is shown in Fig. 13. Numerous pore defects are distributed along the boundary of the LAM repair zone and the fatigue crack traverses the entire leading-edge region and propagates inward. In contrast, only two pores are observed aside from the main fatigue crack in the LAM repaired blade, and the crack remains confined to the interior without reaching

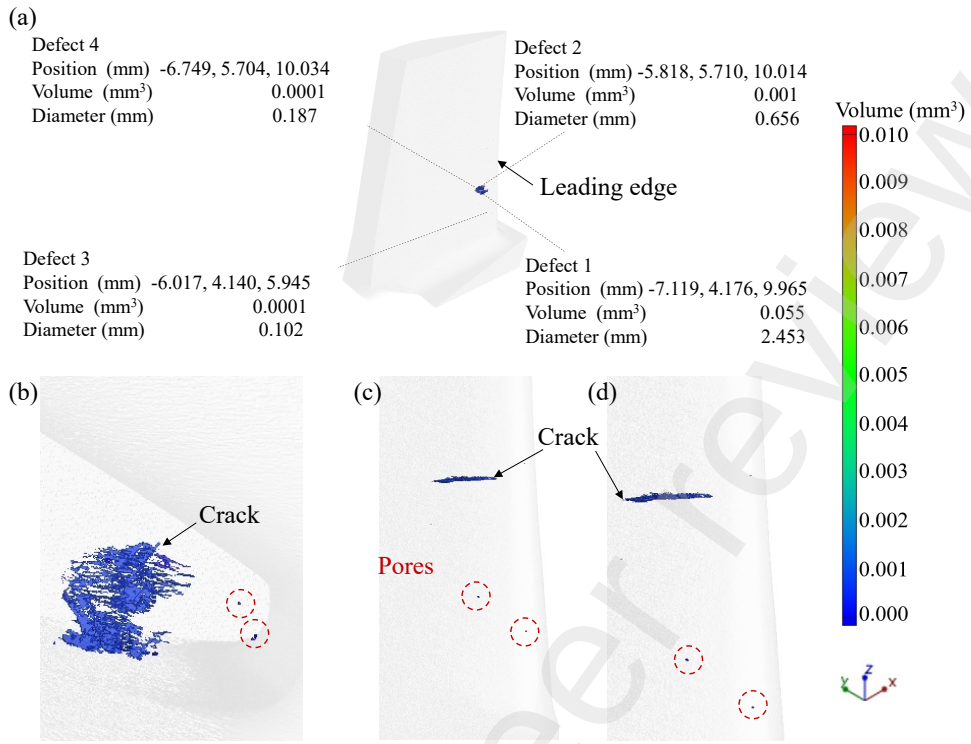

Fig. 13. X-CT scan results showing defect and crack interactions in leading-edge simulated compressor blades:(a) Global view; (b) top view; (c) front view; (d) left view.

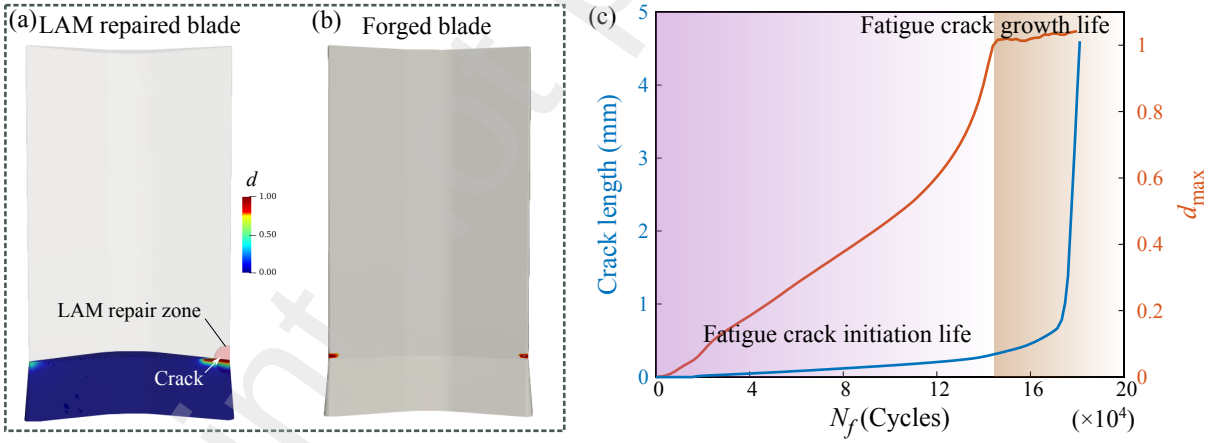

Fig. 14. Phase-field simulation results on fatigue crack initiation and growth life of (a) LAM repaired, (b) forged TC17 blades, and (c) $a - N_f$ curve of LAM repaired blade.

the surface. This observation suggests that fatigue crack initiation may occur within internal defects rather than at the blade leading edge transition cross-section, owing to stress concentrations introduced by LAM repair-induced defects. This variation in defect distribution contributes to the large scatter in the fatigue strength of LAM repaired blades.

Fig. 14 shows the phase-field simulation results of FCG behavior in LAM repaired and forged TC17 blades. The fatigue crack initiation life of the LAM repaired TC17 blade is approximately 144,000 cycles, accounting for more

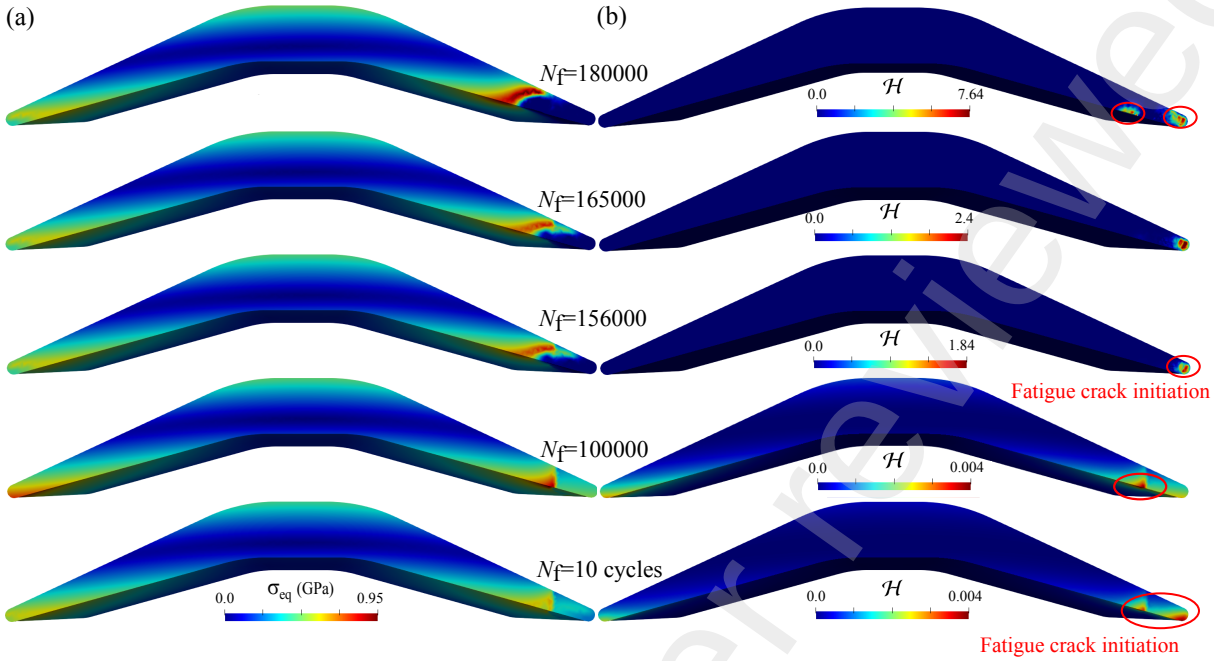

Fig. 15. Phase-field simulation results for the transition cross-section of the LAM repaired simulated compressor blade: (a) Equivalent stress distribution; (b) History-dependent strain energy density.

than 76% of the total fatigue life. In contrast to forged blades, where cracks grow symmetrically, fatigue cracks in LAM repaired blades propagate unilaterally on the repaired side. Fig. 15 shows the phase-field simulation results for fatigue crack initiation in the transition cross-section of the LAM repaired blade. Fatigue crack initiates at the interface between the substrate and LAM repair zone. As shown in Fig. 15a, notable stress concentrations occur in both the unrepaired trailing edge and the repaired leading-edge region. However, the stress concentration is more pronounced in the LAM repair zone, attributed to the elastic mismatch between the substrate and the LAM repair zone. The history-dependent crack driving force (Fig. 15b) initially concentrates on the interface between the substrate and LAM repair zone, as well as along the surface of the leading and trailing edges. This suggests that multiple fatigue initiation sites may exist within the repaired region, with a competitive or coexisting mechanism between the critical point at the blade leading edge and the interface between the LAM repair zone and the substrate. These simulation results align with experimental observations and underscore the critical role of interface defects and the elastic mismatch between the LAM repair zone and substrate in fatigue crack initiation.

4.2.3. Fatigue crack growth

Fig. 16 shows the electronic channel contrast (ECC) image of the main crack located on the concave side of the leading edge of the LAM repaired TC17 blade. The crack length is approximately 5 mm, extending across the repair region and into the substrate. The main crack exhibits a curved growth path. Notably, compared with the substrate zone, the crack growth in the LAM repair zone exhibits more pronounced bifurcation and deflection behavior. As shown in Fig. 16b, multiple secondary cracks are observed along the main crack path in the LAM repair zone, whereas such features are rarely observed in the substrate zone. The microstructure in the LAM repair zone consists entirely of coarse prior β phase. Accordingly, a single crack propagation mode is observed, crossing prior β phase, as shown in Fig. 16c and d. This indicates that the fatigue failure mechanism in the LAM repair zone of TC17 blade is governed by transgranular fracture.

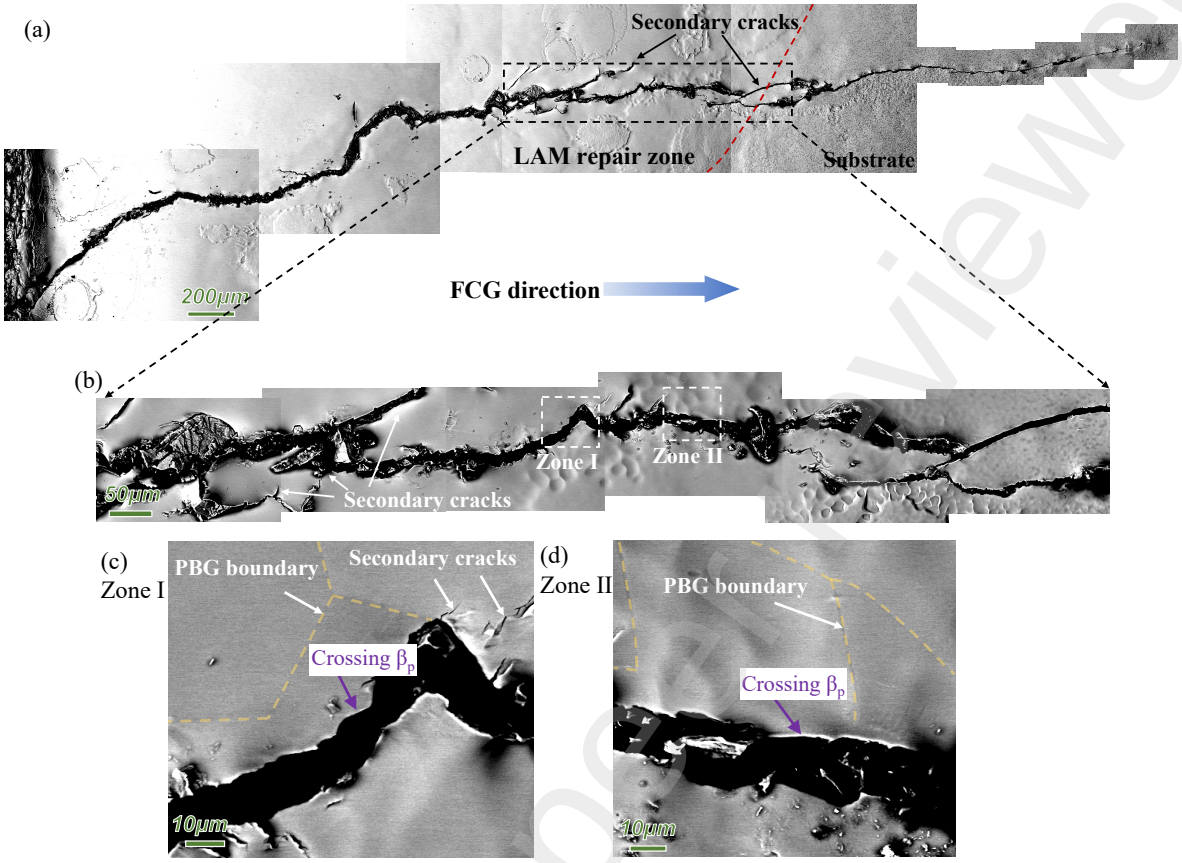

Fig. 16. (a) Global ECC image of leading edge crack in the LAM repaired blade. (b) Fatigue crack growth in LAM repair zone. (c) High magnification image of zone I. (d) High magnification image of zone II.

Fig. 17 shows the phase-field evolution of the damage variable D and the crack order parameter d in the LAM repaired blade under periodic aerodynamic loading and centrifugal static loading. In phase-field simulation, fatigue cracks initiate near the interface between the substrate and the LAM repair zone, close to the blade root, and preferentially grow within the LAM repair zone. In contrast to the unrepaired intact blades, where fatigue cracks initiate and propagate on the critical surfaces at both ends of the blade, fatigue damage in the LAM repaired blades is localized within the repaired region. In addition, the phase-field simulation accurately captures the 3D FCG path and fracture surface morphology in the LAM repaired blade, exhibiting good agreement with the X-CT observations (Fig. 18). The fatigue crack in the LAM repaired compressor blade grows to a length of 4.6 mm at failure (N_f = 180,000 cycles), which is close to the experimentally measured critical crack length of a_c = 5 mm. With defect effects macroscopically considered, defect-related fatigue damage accumulation and the associated crack driving force play a critical role in the FCG process.

The crack front varies along the height of the cross-section, as shown in Fig. 19. Our phase-field simulation successfully reproduces these experimental observations. At h = 10 mm (the transition cross-section), the crack surface spans the entire LAM repair zone, while at h = 11 mm, the crack front exhibits a serrated morphology. The phase-field framework incorporating the defect-based fatigue model has been validated through the practical simulation of 3D FCG behavior in the LAM repaired TC17 specimens and component. The agreement between simulation and experiment highlights the model's robustness in predicting fatigue crack initiation, growth direction,

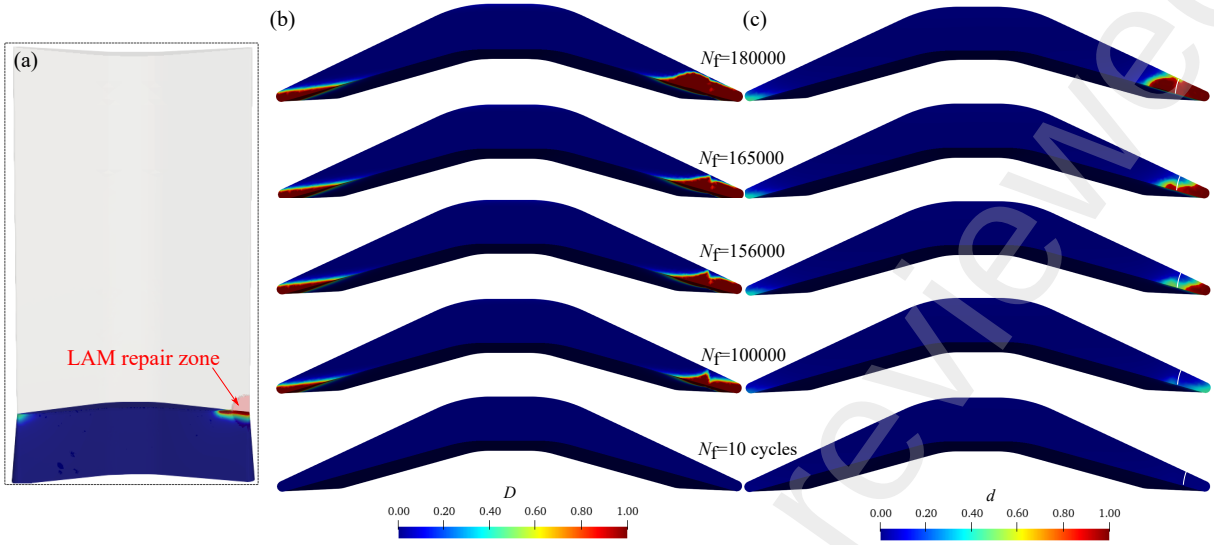

Fig. 17. Phase-field simulation results of (a) global crack evolution, (b) phase-field damage variable D distribution, and (c) crack d in dangerous cross section in the LAM repaired blade.

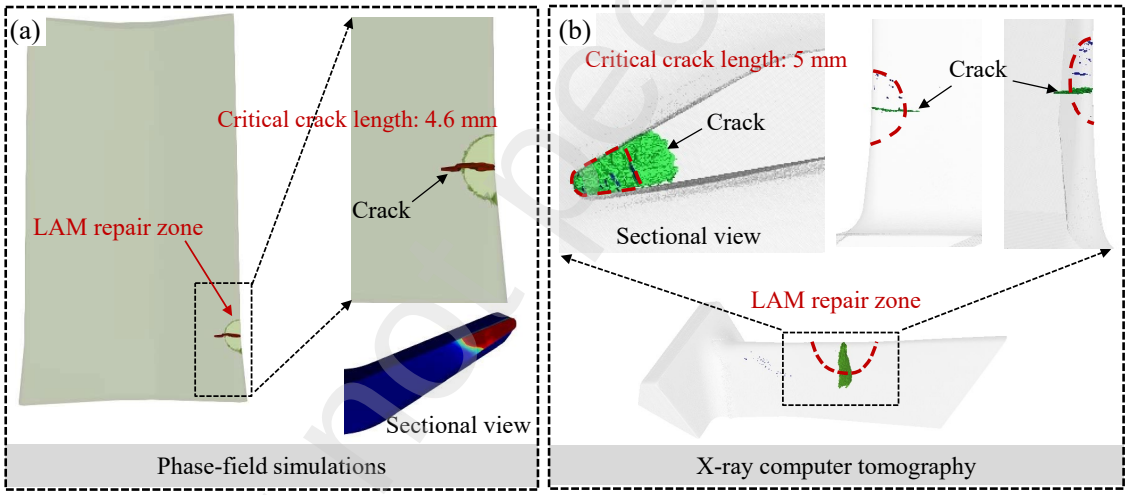

Fig. 18. Fatigue crack growth behavior by (a) phase-field simulation and (b) experiment.

and front morphology under realistic loading conditions.

4.3. Fatigue Strength

Vibration-based bending fatigue tests are conducted on the unrepaired and LAM repaired TC17 blades using a stepwise loading method, as shown in Subsection 2.3. Vibration-based bending fatigue results of unrepaired and LAM repaired blades with a 3 mm semicircular notch is summarized in Table A.3. Compared to the undamaged forged TC17 blades, the high-cycle fatigue strength of the LAM repaired blades (at 3×10^7 cycles) is decreased by 52.4% to 65.6%. This significant reduction is primarily attributed to the elevated crack growth rate caused by coarse prior β phase and the presence of manufacturing defects such as LOF or pores (Kanishka and Acherjee, 2023; Wang et al., 2024). However, compared to blades subjected to FOD, the fatigue strength of the LAM repaired blades

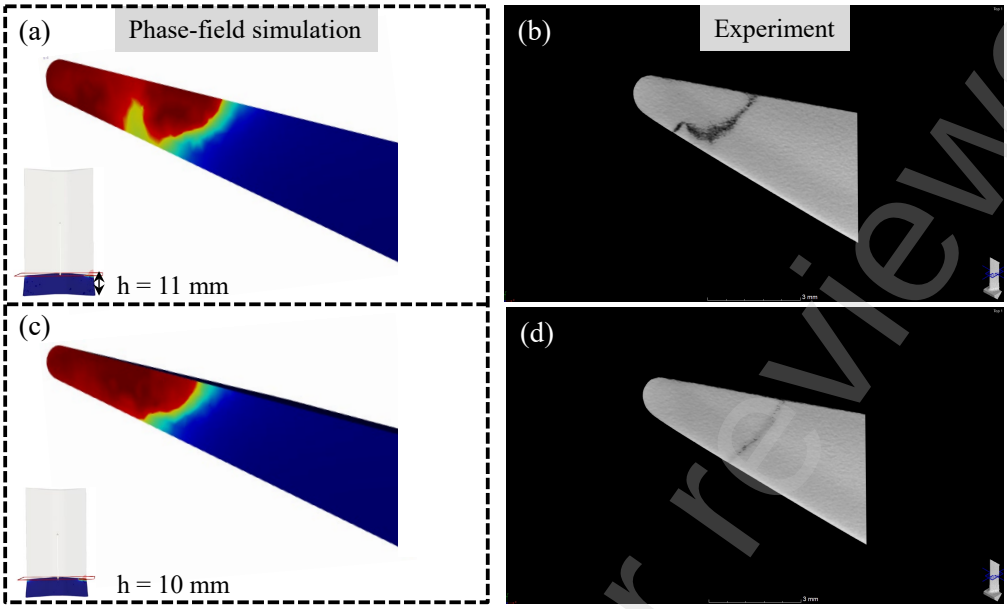

Fig. 19. Crack order parameter profiles with (a,c) phase-field simulation and (b,d) X-CT experiment of leading edge of the LAM repaired compressor blade under various dangerous sections.

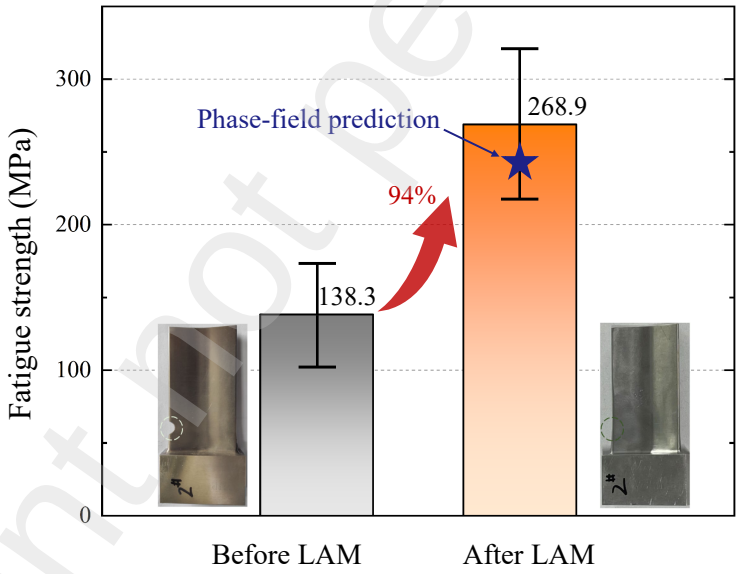

Fig. 20. Fatigue strength of LAM repaired TC17 blades obtained from experiments and phase-field simulations. The experimental fatigue strength of the FOD-notched blade is taken from Ref. (Zhang, 2020).

increased by 94%, demonstrating the strong fatigue performance recovery provided by LAM repair.

Based on phase-field simulations of the LAM repaired blades, the predicted fatigue strength and critical crack length are 241 MPa and 4.6 mm, respectively, as summarized in Table 2. These results show relative errors of 10.4% and 8% when compared with experimental data. The phase-field framework, incorporating pore defects information, demonstrates a reasonable capability for predicting fatigue performance, and accurately reproduces the fatigue crack initiation and growth behavior observed in the LAM repaired blade experiments.

Table 2. Experimental and phase-field simulation results for LAM repaired TC17 blade (3 mm semicircle notch).

	Experiment	Phase-field simulation	Relative error
Fatigue strength (MPa)	268.9	241	10.4%
Critical crack length (mm)	5	4.6	8%

5. Conclusion

In summary, we have demonstrated the fatigue performance restoration and failure mechanisms in LAM repaired titanium-alloy blades through the combination of experiments and phase-field modeling. Vibration-based bending fatigue tests, combined with SEM and X-CT, are performed to evaluate the fatigue strength after LAM repair and to characterize LAM repair-induced pore defects. The influence of these pore defects on the FCG behavior of LAM repaired blades is assessed. In order to predict the FCG behavior and fatigue strength of LAM repaired blades, a phase-field fatigue fracture model considering LAM repair-induced defect features (including defect size, location and sphericity) is proposed. It is demonstrated, both experimentally and numerically, that LAM repair-induced pore defects have a strong impact on the resulting fatigue performance, and the phase-field model prediction agrees well the experimental results.

X-CT results show that the LAM repair-induced defects are dominated by near-spherical pore defects, with over 90% exhibiting an equivalent diameter below 60 μm, and are primarily distributing at the interface between the substrate and the LAM repair zone. It is found that these internal defects serve as fatigue crack initiation sites and significantly affect fatigue resistance. This contrasts with the forged blade, in which the crack initiates at the arc-shaped surface of the leading edge and propagates into the interior of the blade. The fatigue strength after LAM repair improved by 94% when compared to the notched blades, confirming the fatigue performance restoration potential by LAM repair. These behaviors are well captured by our phase-field model incorporating fatigue life model that considers the LAM repair-induced pore defects. The fatigue life predictions of LAM repaired TC17 fatigue specimens fall within the ±2 times error band. In the case of LAM repaired TC17 compressor blades, the critical fatigue crack length (a_c = 4.6 mm) and fatigue strength (σ_e = 241 MPa) predicted by phase-field model agree well with the fatigue experimental results (a_c = 5 mm and σ_e = 268.9 MPa), with relative errors below 11%. Furthermore, the phase-field simulations reproduce the 3D fatigue crack initiation and propagation behaviors, as well as fracture surface morphology observed in experiments, validating the phase-field model's predictive capability for LAM repaired metallic components.

Informed by experiments, our phase-field model framework here provides a practicable toolkit for rapid evaluation of fatigue performance of LAM repaired metallic components, as well as for the computational prediction and design of pore-sensitive components. Future research could build upon this framework by integrating realistic pore defect reconstruction from X-CT (Wu et al., 2017) and considering defect evolution, thereby enhancing its predictive capability and broadening its engineering relevance in LAM repaired metallic components.

CRediT authorship contribution statement

Wei Tang: Formal analysis, Investigation, Visualization, Funding acquisition, Data curation, Writing – original draft. **Lingfeng Wang**: Writing – review & editing, Investigation, Formal analysis, Data curation. **Shen Sun**: Investigation, Formal analysis, Data curation. **Liucheng Zhou**: Conceptualization, Supervision, Writing – review & editing. **Marco Paggi**: Conceptualization, Resources, Supervision, Writing – review & editing. **Min Yi**: Formal anal-

ysis, Investigation, Conceptualization, Resources, Supervision, Project administration, Funding acquisition, Writing – original draft & review & editing.

Declaration of competing interest

The authors declare that they have no known competing financial interests or personal relationships that could have appeared to influence the work reported in this paper.

Acknowledgements

The authors acknowledge the support from National Science and Technology Major Project (J2019-IV-0014-0082), Outstanding Youth Fund of Jiangsu Province (BK20240077), Key Project (Provincial-Municipal Joint) of Jiangsu Province (BK20243044), State Key Laboratory of Mechanics and Control for Aerospace Structures (MCAS-S-0124K02), Fundamental Research Funds for the Central Universities (NE2024001), National Key Research and Development Program of China (2022YFB4600700), Funding for Outstanding Doctoral Dissertation (BCXJ25-03) in NUAA, National Youth Talents Program of China, and a project Funded by the Priority Academic Program Development of Jiangsu Higher Education Institutions.

References

Alessi, R., Vidoli, S., De Lorenzis, L., 2018. A phenomenological approach to fatigue with a variational phase-field model: The one-dimensional case. Engineering Fracture Mechanics 190, 53–73. doi:10.1016/j.engfracmech.2017.11.036.

Amor, H., Marigo, J.J., Maurini, C., 2009. Regularized formulation of the variational brittle fracture with unilateral contact: Numerical experiments. Journal of the Mechanics and Physics of Solids 57, 1209–1229. doi:10.1016/j.jmps.2009.04.011.

Anatolyevich, B.P., Yakovlevna, G.N., 2019. Generalization of the ramberg–osgood model for elastoplastic materials. Journal of Materials Engineering and Performance 28, 7342–7346.

Borden, M.J., Hughes, T.J., Landis, C.M., Anvari, A., Lee, I.J., 2016. A phase-field formulation for fracture in ductile materials: Finite deformation balance law derivation, plastic degradation, and stress triaxiality effects. Computer Methods in Applied Mechanics and Engineering 312, 130–166. doi:10.1016/j.cma.2016.09.005.

Bourdin, B., Francfort, G.A., Marigo, J.J., 2000. Numerical experiments in revisited brittle fracture. Journal of the Mechanics and Physics of Solids 48, 797–826.

Braides, A., 1998. Approximation of free-discontinuity problems. 1694, Springer Science & Business Media.

Carrara, P., Ambati, M., Alessi, R., De Lorenzis, L., 2020. A framework to model the fatigue behavior of brittle materials based on a variational phase-field approach. Computer Methods in Applied Mechanics and Engineering 361, 112731. doi:10.1016/j.cma.2019.112731.

Cavuoto, R., Lenarda, P., Tampieri, A., Bigoni, D., Paggi, M., 2024. Phase-field modelling of failure in ceramics with multiscale porosity. Materials and Design 238, 112708. doi:10.1016/j.matdes.2024.112708.

Chen, Y., Yin, Y., Yi, M., 2024. Powder bed fusion repair of titanium with surface damage: Molecular dynamics study on microstructure and mechanical properties. Additive Manufacturing 84, 104096. doi:https://doi.org/10.1016/j.addma.2024.104096.

Cui, C., Ma, R., Martínez-Pañeda, E., 2022. A generalised, multi-phase-field theory for dissolution-driven stress corrosion cracking and hydrogen embrittlement. Journal of the Mechanics and Physics of Solids 166, 104951. doi:10.1016/j.jmps.2022.104951.

Darabi, R., Azinpour, E., Reis, A., Sa, J.C.d., 2024. Elasto-plastic phase-field analysis of thermal induced-cracking and its application towards metal additive manufacturing. European Journal of Mechanics - A/Solids 107, 105369. doi:https://doi.org/10.1016/j.euromechsol.2024.105369.

Darabi, R., Gil, J.W., Azinpour, E., Sousa, J., Reis, A., de Sá, J.C., 2025. Controlling hot cracking in wc–nicrbsife coatings produced by laser surface cladding: A multiphase field approach for enhancing process repeatability. Journal of the Mechanics and Physics of Solids , 106238.

Denkena, B., Boess, V., Nespor, D., Floeter, F., Rust, F., 2015. Engine blade regeneration: a literature review on common technologies in terms of machining. The International Journal of Advanced Manufacturing Technology 81, 917–924.

Ge, X., Ma, Y., Zhou, L., Li, W., 2023. Modelling the anisotropic fracture behaviour of cold spray additive manufactured 6061 aluminium alloy deposits based on the phase field method. Additive Manufacturing , 103932doi:10.1016/j.addma.2023.103932.

Han, H., Wang, T., Huang, G., Liu, Z., Zhuang, Z., 2024. Study of the dynamic impact spalling of ductile materials based on Gurson-type phase-field model. International Journal of Plasticity 181, 104106. doi:10.1016/j.ijplas.2024.104106.

Hu, W., Yi, M., 2024. Predicting tensile behavior and fatigue life of laser shock peened titanium alloy by crystal plasticity model. International Journal of Fatigue 187, 108476.

Hu, Y., Wu, S., Xie, C., Wu, W., Zhang, J., 2021. Fatigue life evaluation of Ti–6Al–4V welded joints manufactured by electron beam melting. Fatigue & Fracture of Engineering Materials & Structures 44, 2210–2221.

Hu, Y.N., Wu, S.C., Withers, P.J., Zhang, J., Bao, H.Y., Fu, Y.N., Kang, G.Z., 2020. The effect of manufacturing defects on the fatigue life of selective laser melted Ti-6Al-4V structures. Materials and Design 192. doi:10.1016/j.matdes.2020.108708.

Jie, Z., Wang, W., Chen, C., Wang, K., 2021. Local approaches and xfem used to estimate life of cfrp repaired cracked welded joints under fatigue loading. Composite Structures 260, 113251. doi:https://doi.org/10.1016/j.compstruct.2020.113251.

Jones, R., Chen, F., Pitt, S., Paggi, M., Carpinteri, A., 2016. From nasgro to fractals: Representing crack growth in metals. International Journal of Fatigue 82, 540–549. doi:10.1016/j.chaos.2007.08.068.

Kalina, M., Linse, T., Hantschke, P., Kästner, M., 2020. An efficient phase-field model for fatigue fracture in ductile materials. Engineering Fracture Mechanics 224, 106807. doi:10.1016/j.engfracmech.2019.106807.

Kalina, M., Schöne, V., Spak, B., Paysan, F., Breitbarth, E., Kästner, M., 2023. Fatigue crack growth in anisotropic aluminium sheets – phase-field modelling and experimental validation. International Journal of Fatigue 176, 107874. doi:10.1016/j.ijfatigue.2023.107874.

Kanishka, K., Acherjee, B., 2023. A systematic review of additive manufacturing-based remanufacturing techniques for component repair and restoration. Journal of Manufacturing Processes 89, 220–283. doi:10.1016/j.jmapro.2023.01.034.

Li, C., Fang, J., Wan, Y., Qiu, N., Steven, G., Li, Q., 2023a. Phase field fracture model for additively manufactured metallic materials. International Journal of Mechanical Sciences 251, 108324. doi:10.1016/j.ijmecsci.2023.108324.

Li, C., Fang, J., Wu, C., Sun, G., Steven, G., Li, Q., 2022a. Phase field fracture in elasto-plastic solids: Incorporating phenomenological failure criteria for ductile materials. Computer Methods in Applied Mechanics and Engineering 391, 114580. doi:10.1016/j.cma.2022.114580.

Li, C., Liu, J., Dong, L., Wu, C., Steven, G., Li, Q., Fang, J., 2025. Phase field fracture in elastoplastic solids: a stress-state, strain-rate, and orientation dependent model in explicit dynamics and its applications to additively manufactured metals. Journal of the Mechanics and Physics of Solids 197, 105978. doi:10.1016/j.jmps.2024.105978.

Li, H., Tian, Z., Zheng, J., Huang, K., Nie, B., Xu, W., Zhao, Z., 2023b. A defect-based fatigue life estimation method for laser additive manufactured Ti-6Al-4V alloy at elevated temperature in very high cycle regime. International Journal of Fatigue 167, 107375. doi:10.1016/j.ijfatigue.2022.107375.

Li, P., Yvonnet, J., Combescure, C., Makich, H., Nouari, M., 2021. Anisotropic elastoplastic phase field fracture modeling of 3D printed materials. Computer Methods in Applied Mechanics and Engineering 386, 114086. doi:10.1016/j.cma.2021.114086.

Li, Z.J., Wang, T., Chu, D.Y., Liu, Z.L., Cui, Y.N., 2022b. A coupled crystal-plasticity and phase-field model for understanding fracture behaviors of single crystal tungsten. International Journal of Plasticity 157. doi:10.1016/j.ijplas.2022.103375.

Ling, W., Wang, X., Gao, Q., Gao, Z., Wang, X., Zhan, X., 2024. Toward developing remanufactured ti6al4v alloys with high fatigue crack growth resistance by in-situ cooling during laser remanufacturing. International Journal of Fatigue 187, 108455. doi:https://doi.org/10.1016/j.ijfatigue.2024.108455.

Liu, Q., Wang, Y., Zheng, H., Tang, K., Li, H., Gong, S., 2016. TC17 titanium alloy laser melting deposition repair process and properties. Optics & Laser Technology 82, 1–9. doi:https://doi.org/10.1016/j.optlastec.2016.02.013.

Liu, Y.K., Fan, J.L., Zhu, G., Zhu, M.L., Xuan, F.Z., 2023. Data-driven approach to very high cycle fatigue life prediction. Engineering Fracture Mechanics 292, 109630. doi:10.1016/j.engfracmech.2023.109630.

Loiodice, L., Stopka, K.S., Sangid, M.D., 2025. Pore defects' influence on the local, near threshold fatigue crack growth behavior of additively manufactured Ti-6Al-4V. Journal of the Mechanics and Physics of Solids 202, 106173. doi:10.1016/j.jmps.2025.106173.

Lourenço, J.M., Da Sun, S., Sharp, K., Luzin, V., Klein, A.N., Wang, C.H., Brandt, M., 2016. Fatigue and fracture behavior of laser clad repair of aermet® 100 ultra-high strength steel. International Journal of Fatigue 85, 18–30.

Mattey, R., Jewell, B., Ghosh, S., Sain, T., 2023. Phase-field fracture coupled elasto-plastic constitutive model for 3D printed thermoplastics and composites. Engineering Fracture Mechanics 291, 109535. doi:10.1016/j.engfracmech.2023.109535.

Maxwell, D.C., Nicholas, T., 1999. A rapid method for generation of a haigh diagram for high cycle fatigue, in: Fatigue and Fracture Mechanics: 29th Volume. ASTM International.

Mi, C., Li, Y., Xiao, Y., Li, H., Xu, L., Tang, J., 2025. Fatigue fracture analysis and lifetime prediction of laser-cladded notched titanium alloy based on energy dissipation method. International Journal of Damage Mechanics doi:10.1177/10567895251358290.

Miehe, C., Hofacker, M., Welschinger, F., 2010. A phase field model for rate-independent crack propagation: Robust algorithmic implementation based on operator splits. Computer Methods in Applied Mechanics and Engineering 199, 2765–2778. doi:10.1016/j.cma.2010.04.011.

Miehe, C., Schaenzel, L.M., Ulmer, H., 2015. Phase field modeling of fracture in multi-physics problems. Part I. Balance of crack surface and failure criteria for brittle crack propagation in thermo-elastic solids. Computer Methods in Applied Mechanics and Engineering 294, 449–485. doi:10.1016/j.cma.2014.11.016.

Miner, M.A., 1945. Cumulative damage in fatigue. Journal of Applied Mechanics 12, A159–A164. doi:10.1115/1.4009458.

Molina, C., Araujo, A., Bell, K., Mendez, P.F., Chapetti, M., 2021. Fatigue life of laser additive manufacturing repaired steel component. Engineering Fracture Mechanics 241, 107417. doi:10.1016/j.engfracmech.2020.107417.

Mudge, R.P., Wald, N.R., 2007. Laser engineered net shaping advances additive manufacturing and repair. Welding Journal-New York- 86, 44.

Murakami, Y., Kodama, S., Konuma, S., 1989. Quantitative evaluation of effects of non-metallic inclusions on fatigue strength of high strength steels. I: Basic fatigue mechanism and evaluation of correlation between the fatigue fracture stress and the size and location of non-metallic inclusions. International Journal of Fatigue 11, 291–298.

Murakami, Y., Usuki, H., 1989. Quantitative evaluation of effects of non-metallic inclusions on fatigue strength of high strength steels. II: Fatigue limit evaluation based on statistics for extreme values of inclusion size. International Journal of Fatigue 11, 299–307.

Nagalingam, A.P., Gopasetty, S.K., Wang, J., Yuvaraj, H.K., Gopinath, A., Yeo, S., 2023. Comparative fatigue analysis of wrought and laser powder bed fused Ti-6Al-4V for aerospace repairs: Academic and industrial insights. International Journal of Fatigue 176, 107879. doi:https://doi.org/10.1016/j.ijfatigue.2023.107879.

Neuber, H., 1961. Theory of Stress Concentration for Shear-Strained Prismatical Bodies With Arbitrary Nonlinear Stress-Strain Law. Journal of Applied Mechanics 28, 544–550. doi:10.1115/1.3641780.

Paydas, H., Mertens, A., Carrus, R., Lecomte-Beckers, J., Tchoufang Tchuindjang, J., 2015. Laser cladding as repair technology for Ti–6Al–4V alloy: Influence of building strategy on microstructure and hardness. Materials & Design 85, 497–510. doi:https://doi.org/10.1016/j.matdes.2015.07.035.

Plekhov, O., Paggi, M., Naimark, O., Carpinteri, A., 2011. A dimensional analysis interpretation to grain size and loading frequency dependencies of the paris and wöhler curves. International journal of fatigue 33, 477–483. doi:10.1016/j.ijfatigue.2010.10.001.

Ruan, H., Rezaei, S., Yang, Y., Gross, D., Xu, B.X., 2023. A thermo-mechanical phase-field fracture model: Application to hot cracking simulations in additive manufacturing. Journal of the Mechanics and Physics of Solids 172, 105169. doi:10.1016/j.jmps.2022.105169.

Sarkar, R., Chen, B., Fitzpatrick, M.E., Fabijanic, D., Hilditch, T., 2022. Additive manufacturing-based repair of in718 superalloy and high-cycle fatigue assessment of the joint. Additive Manufacturing 60, 103276. doi:https://doi.org/10.1016/j.addma.2022.103276.

Sun, G., Zhou, R., Lu, J., Mazumder, J., 2015. Evaluation of defect density, microstructure, residual stress, elastic modulus, hardness and strength of laser-deposited aisi 4340 steel. Acta Materialia 84, 172–189. doi:https://doi.org/10.1016/j.actamat.2014.09.028.

Sun, S., Gong, Q., Ni, Y., Yi, M., 2024. A micromagnetic-mechanically coupled phase-field model for fracture and fatigue of magnetostrictive alloys. Journal of the Mechanics and Physics of Solids , 105767doi:10.1016/j.jmps.2024.105767.

Sun, S., Liu, S., He, W., Zhang, X., Tang, W., Zhou, L., Yi, M., 2025. Predicting high-cycle fatigue strength and three-dimensional fatigue crack growth in simulated compressor blade by phase-field model. Aerospace Science and Technology 159, 110009. doi:10.1016/j.ast.2025.110009.

Sun, S.D., Liu, Q., Brandt, M., Luzin, V., Cottam, R., Janardhana, M., Clark, G., 2014. Effect of laser clad repair on the fatigue behaviour of ultra-high strength AISI 4340 steel. Materials Science and Engineering: A 606, 46–57. doi:https://doi.org/10.1016/j.msea.2014.03.077.

Talebi, B., Abedian, A., 2016. Numerical modeling of adhesively bonded composite patch repair of cracked aluminum panels with concept of CZM and XFEM. Proceedings of the Institution of Mechanical Engineers, Part G: Journal of Aerospace Engineering 230, 1448–1466.

Tang, W., Su, S., Sun, S., Liu, S., Yi, M., 2025. Phase-field modeling for predicting three-dimensional fatigue crack initiation and growth under laser shock peening induced residual stress. International Journal of Fatigue 193, 108786. doi:10.1016/j.ijfatigue.2024.108786.

Tang, W., Tang, Z., Lu, W., Wang, S., Yi, M., 2023. Modeling and prediction of fatigue properties of additively manufactured metals. Acta Mechanica Solida Sinica 36, 181–213. doi:10.1007/s10338-023-00380-5.

Tang, W., Yi, M., Chen, L.Q., Guo, W., 2024. Classical fatigue theory informed phase-field model for high-cycle fatigue life and fatigue crack growth. Engineering Fracture Mechanics 306, 110212. doi:10.1016/j.engfracmech.2024.110212.

Tomlinson, K., Fletcher, D., Lewis, R., 2023. Evaluation of laser cladding as an in-situ repair method on rail steel. Tribology International 180, 108210. doi:https://doi.org/10.1016/j.triboint.2022.108210.

Tonks, M.R., Gaston, D., Millett, P.C., Andrs, D., Talbot, P., 2012. An object-oriented finite element framework for multiphysics phase field simulations. Computational Materials Science 51, 20–29. doi:10.1016/j.commatsci.2011.07.028.

Tran, H.S., Tchuindjang, J.T., Paydas, H., Mertens, A., Jardin, R., Duchêne, L., Carrus, R., Lecomte-Beckers, J., Habraken, A., 2017. 3d thermal finite element analysis of laser cladding processed ti-6al-4v part with microstructural correlations. Materials & Design 128, 130–142.

Walker, K., Lourenço, J., Sun, S., Brandt, M., Wang, C., 2017. Quantitative fractography and modelling of fatigue crack propagation in high strength aermet®100 steel repaired with a laser cladding process. International Journal of Fatigue 94, 288–301. doi:https://doi.org/10.1016/j.ijfatigue.2016.06.031. fatigue and Fracture Behavior of Additive Manufactured Parts.

Wang, L., Li, Y., Zhou, L., Lou, Y., Liu, S., Zheng, D., Yi, M., 2023a. Progress in additive manufacturing, additive repair and fatigue evaluation of aviation titanium alloy blades. Materials Research Letters 11, 973–1012. doi:10.1080/21663831.2023.2275599.

Wang, L., Luo, S., Lu, K., Zhang, X., Zhao, Z., Liu, P., Yi, M., Zhou, L., 2024. Effect of laser additive repair on high cycle fatigue properties of TC17 titanium alloy. International Journal of Fatigue 178, 108026. doi:10.1016/j.ijfatigue.2023.108026.

Wang, X., Xu, L., Zhao, L., Han, Y., 2023b. Defect-related strain-controlled high-temperature fatigue behavior in additive manufacturing Hastelloy X assisted with ultrasonic micro-forging treatment. International Journal of Fatigue 172, 107607. doi:10.1016/J.IJFATIGUE.2023.107607.

Wu, S., Xiao, T., Withers, P., 2017. The imaging of failure in structural materials by synchrotron radiation X-ray microtomography. Engineering Fracture Mechanics 182, 127–156.

Xie, B., Yu, T., Li, R., Luo, Z., Baxevanakis, K.P., Zhang, P., 2025. Experimentally validated macro-mesoscopic simulation study on the fatigue short crack initiation and propagation in polycrystalline structure utilizing cp-xfem. Engineering Fracture Mechanics 319, 110995.

Xu, B., Yu, C., Wang, C., Kan, Q., Wang, Q., Kang, G., 2024. Effect of pore on the deformation behaviors of NiTi shape memory alloys: A crystal-plasticity-based phase field modeling. International Journal of Plasticity 175. doi:10.1016/j.ijplas.2024.103931.

Zan, X., Guo, X., Weng, G., 2025. Simulation of fracture behaviors in hydrogenated zirconium alloys using a crystal plasticity coupled phase-field fracture model. International Journal of Plasticity 188, 104304.

Zhan, M.J., Sun, G.F., Wang, Z.D., Shen, X.T., Yan, Y., Ni, Z.H., 2019. Numerical and experimental investigation on laser metal deposition as repair technology for 316L stainless steel. Optics and Laser Technology 118, 84–92. doi:10.1016/j.optlastec.2019.05.011.

Zhang, J., 2020. Study on Prediction Method of High Cycle Fatigue Strength of TC17 Titanium Alloy Blade with Foreign Object Damage. Master's thesis. Nanjing University of Aeronautics and Astronautics.

Zhou, S., An, J., Wang, X., Xie, L.y., Xu, X., 2022. Study on fatigue crack propagation behavior of TA15 titanium alloy repaired by laser deposition repair. Fatigue & Fracture of Engineering Materials & Structures 45, 3692–3700.

Zhou, S., Yu, H., An, J., Wang, X., Wang, Z., Xie, L., Hu, Z., Zhao, B., 2024. Study on fatigue crack growth behavior of the TA15 titanium alloy repaired by laser deposition. Engineering Failure Analysis 161, 108276. doi:https://doi.org/10.1016/j.engfailanal.2024.108276.

Zhu, M.L., Jin, L., Xuan, F.Z., 2018. Fatigue life and mechanistic modeling of interior micro-defect induced cracking in high cycle and very high cycle regimes. Acta Materialia 157, 259–275. doi:10.1016/j.actamat.2018.07.036.

Zhu, Y., Yang, Y., Mu, X., Wang, W., Yao, Z., Yang, H., 2019. Study on wear and RCF performance of repaired damage railway wheels: Assessing laser cladding to repair local defects on wheels. Wear 430-431, 126–136. doi:https://doi.org/10.1016/j.wear.2019.04.028.

Appendix A. High-cycle fatigue strength

In the vibration-based bending fatigue test, the measure of fatigue strength of the LAM repaired simulated blade can be obtain, i.e.,

$$\frac{\sigma_{\mathrm{D,s}}}{\sigma_{\mathrm{D,t}}} = \frac{\sigma_{\mathrm{P,s}}}{\sigma_{\mathrm{P,t}}} = \frac{\sigma_{\mathrm{max,s}}}{\sigma_{\mathrm{max,t}}} \tag{A.1}$$

Table A.3. Vibration-based bending fatigue results of unrepaired (Zhang, 2020) and LAM repaired blades with a 3 mm semicircular notch.

Category	ID	σ_e (MPa)	Average (MPa)	Category	σ_e (MPa)	Average (MPa)
Unrepaired blades	1	150.54	138.34	LAM repaired blades	273.99	268.90
	2	192.87			367.47	
	3	150.34			212.89	
	4	150.18			218.71	
	5	151.62			307.00	
	6	149.82			264.16	
	7	122.80			278.68	
	8	70.72			294.36	
	9	100.70			176.32	
	10	139.46			214.80	
	11	150.66			318.14	
	12	130.33			300.24	

There is a relationship between the true results and the simulation results. In the range of low stress and high cycle fatigue, the test results of displacement and stress have high linearity. The fatigue strength is viewed as the maximum stress at leading edge of blade specimen ($\sigma_{max,t}$). The simulated modal stress at D point ($\sigma_{D,s}$) and the maximum stress at leading edge ($\sigma_{max,s}$) are calculated by FE simulations. The trued stress at P point $\sigma_{P,t}$ is obtained via Hooke's law the measured strain. Points D and P are located as shown in Fig. 3. Herein, the ratio of $\sigma_{max,s}$ to $\sigma_{P,s}$ is 5.13 via FE simulations. High-cycle fatigue results of unrepaired and LAM repaired blades with a 3 mm semicircular notch is summarized in Table A.3.